



Review

Solid oxide electrolysis cell analysis by means of electrochemical impedance spectroscopy: A review



A. Néchache*, M. Cassir, A. Ringuedé*

Laboratoire d'Électrochimie, Chimie des Interfaces et Modélisation pour l'Énergie LECIME, UMR 7575 CNRS, Chimie-ParisTech, PSL, 11 rue Pierre et Marie Curie, F-75005 Paris, France

HIGHLIGHTS

- High temperature water electrolysis is a promising solution to produce hydrogen.
- Use of EIS to characterize SOEC electrodes is reviewed.
- EIS as a tool for SOEC degradation in different cell configurations is also reviewed.
- Implementation of a systematic SOEC analysis based on EIS is introduced.

ARTICLE INFO

Article history:

Received 17 October 2013

Received in revised form

17 January 2014

Accepted 23 January 2014

Available online 4 March 2014

Keywords:

Solid oxide electrolysis cell

Electrochemical impedance spectroscopy

High temperature electrolysis

Electrochemical mechanisms

Degradation

ABSTRACT

High temperature water electrolysis based on Solid Oxide Electrolysis Cell (SOEC) is a very promising solution to produce directly pure hydrogen. However, degradation issues occurring during operation still represent a scientific and technological barrier in view of its development at an industrial scale. Electrochemical Impedance Spectroscopy (EIS) is a powerful *in-situ* fundamental tool adapted to the study of SOEC systems. Hence, after a quick presentation of EIS principle and data analysis methods, this review demonstrates how EIS can be used: (i) to characterize the performance and mechanisms of SOEC electrodes; (ii) as a complementary tool to study SOEC degradation processes for different cell configurations, in addition to post-test tools such as scanning electron microscopy (SEM) or X-ray diffraction (XRD). The use of EIS to establish a systematic SOEC analysis is introduced as well.

© 2014 Elsevier B.V. All rights reserved.

1. Introduction

Hydrogen is a leading candidate as energy carrier due to its clean, storable and transportable characteristics [1–3]. However, most of current hydrogen production methods such as steam reforming, partial oxidation of heavy hydrocarbons or gasification of coal are based on the use of fossil fuels. Among the various existing processes, water electrolysis, based on the use of water and electricity, is the cleanest way to produce hydrogen. Moreover, increasing the temperature allows: (i) avoiding the use of expensive catalyst such as platinum; (ii) using less electrical energy balanced by more thermal energy which would be at least partly wasted otherwise; (iii) working at higher current densities, meaning generation of important quantities of directly pure hydrogen [1,2,4]. As

shown in Fig. 1, high temperature electrolysis (HTE) can be performed using a solid oxide electrolysis cell (SOEC) which is close to a reversibly operated solid oxide fuel cell (SOFC). The principle of electrolysis explained in Fig. 1 corresponds to the most common used case of an oxide-ion conducting electrolyzer, which differs from the proton-conducting electrolyzer.

The idea of producing hydrogen through high temperature electrolysis of water using a solid oxide electrolyzer cell began to grow during the 1970s [5–8], and one of the first fundamental contributions in this field was made by Badwal [9] who evaluated the potential of urania–yttria fluorite-type solid solutions as electrodes for high temperature electrolysis of water through kinetic studies of oxygen reactions at the $(U_{0.7} Y_{0.3})O_2 + x/YSZ$ interface. However, interest on SOEC really rose during the 1980s as shown by the following mentioned projects and investigations, which represent some of the very first advanced approaches on SOEC. To begin with, Westinghouse Electric Corporation R&D Center, through the studies of Isenberg [10] and Maskalick [11], especially

* Corresponding authors. Tel.: +331 55 42 12 35; fax: +331 44 27 67 50.

E-mail addresses: aziz.nechache@chimie-paristech.fr (A. Néchache), armelle.ringuiede@chimie-paristech.fr (A. Ringuedé).

Abbreviations, symbols and definitions

ADIS	analysis of the difference in impedance spectra	P_{H_2}	hydrogen partial pressure (atm)
BCFN	barium cobalt iron niobium oxide, $BaCo_{0.7}Fe_{0.2}Nb_{0.1}O_3$	P_{H_2O}	water partial pressure (atm)
$- \delta$		P_{O_2}	oxygen partial pressure (atm)
BSCF	barium strontium cobalt ferrite, $Ba_{0.5}Sr_{0.5}Co_{0.8}Fe_{0.2}O_3$	R_p	polarisation resistance (Ω)
$- \delta$		R_s	ohmic resistance (Ω)
C	capacitance (F)	R_{HF}	high frequency resistance ($\Omega\text{ cm}^{-2}$)
CGO	gadolinia-doped ceria, $(Gd,Ce)O_2$	R_{LF}	low frequency resistance ($\Omega\text{ cm}^{-2}$)
C_{HF}	normalized high frequency capacitance ($F\text{ cm}^{-2}$)	R_{MF}	middle frequency resistance ($\Omega\text{ cm}^{-2}$)
C_{MF}	normalized middle frequency capacitance ($F\text{ cm}^{-2}$)	$R//CPE$	resistance-constant phase element parallel circuit
C_{LF}	normalized low frequency capacitance ($F\text{ cm}^{-2}$)	SEM	scanning electron microscopy
C_p	adsorption capacitance (F)	SFM	strontium iron molybdenum oxide, $Sr_2Fe_{1.5}Mo_{0.5}O_6 - \delta$
CPE _{HF}	high frequency constant phase element	SOC	solid oxide cell
CPE _{MF}	middle frequency constant phase element	SOEC	solid oxide electrolysis cell
D	surface diffusivity ($\text{cm}^2\text{ s}^{-1}$)	SOFC	solid oxide fuel cell
DRT	distribution of relaxation time	T	temperature ($^\circ\text{C}$)
EEC	electrical equivalent circuit	TEM	transmission electron microscopy
EDX = EDS	Energy-dispersive X-ray spectroscopy	TPB	triple phase boundary (electrode, electrolyte, gas)
EIS	electrochemical impedance spectroscopy	U	potential (V)
f	frequency (Hz)	XPS	X-ray photoelectron spectroscopy
f_{HF}	high frequency relaxation frequency (Hz)	XRD	X-ray diffraction
f_{LF}	low frequency relaxation frequency (Hz)	YDC	yttria-doped ceria
f_{MF}	middle frequency relaxation frequency (Hz)	YSZ	yttria-stabilized zirconia
GDC	gadolinia-doped ceria, $(Gd,Ce)O_2$	Z_{IM}	$Z'' =$ imaginary impedance (Ω)
H_2 electrode	hydrogen electrode = SOEC cathode where water reduction occurs	Z_R	$Z' =$ real impedance (Ω)
HTE	high temperature electrolysis	ϵ'	real part of the complex relative permittivity (unit less)
i	current density (A cm^{-2})	ϵ''	imaginary part of the complex relative permittivity (unit less)
$i-U$	polarization curve	φ	phase angle, shift ($^\circ$)
I	current (A)	ω	radial frequency (rad)
j	complex number (unit less)	dual	
k	ad/desorption coefficient (s^{-1})	atmosphere	two different gas compositions supplied to the cell, one for the cathode side and one for the anode side
l_δ	utilization length (μm)	half cell	cell composed of an electrode and an electrolyte
LSCo	strontium-doped lanthanum cobaltite, $La_{0.8}Sr_{0.2}CoO_3$	single	
LSCF	strontium-doped ferri-cobaltite, $(La_{1-x}Sr_x)Co_yFe_{1-y}O_{3-\delta}$	atmosphere	one gas composition supplied to the cell
LSCM	strontium-doped lanthanum chromo-manganite, $(La,Sr)(Cr,Mn)O_3$	single	
LSF	strontium-doped lanthanum ferrite, $La_{0.8}Sr_{0.2}FeO_3$	cell	cell composed of two identical or different electrodes with an electrolyte in between, operated in a dual atmosphere
LSGM	lanthanum strontium gallate magnesite, $La_{0.8}Sr_{0.2}Ga_{0.83}Mg_{0.17}O_{3-\delta}$	stack	addition of cells with interconnector plates in between for current collection, atmosphere separation and gas supply
LSM	strontium-doped lanthanum manganite, $La_{0.8}Sr_{0.2}MnO_{3-\delta}$	symmetrical	
Ni–YSZ	metal (nickel) and ceramic (yttria-stabilized zirconia) composite material	cell	cell composed of two identical electrodes with an electrolyte in between. The cell is operated in a single atmosphere
O_2	oxygen electrode = SOEC anode where oxygen oxidation occurs		

reported performance test results of a 7-cell stack composed of Ni–YSZ/YSZ/In₂O₃–YSZ cells [10] and performance characterization of a LSM/YSZ/Ni–YSZ cell [11], respectively. These studies included stable electrolysis at 1000 °C and $P_{H_2O}/P_{H_2} = 5$ with 1.64 V at up to -1.6 A cm^{-2} [10], and a cell voltage of 1.23 V at -0.3 A cm^{-2} [11]. A review of the progress in water electrolysis was given by Imarisio at the end of the first hydrogen program on the European Community [12]. This review includes performance obtained at high temperature, with a cell voltage of about 1.5 V at -1 A cm^{-2} after 1000 h operation at 900 °C, with $P_{H_2O}/P_{H_2} = 5$. Barbi and Mari also contributed to the progress of research in this field. Indeed, after reviewing the high temperature reduction kinetic processes for O₂ and H₂O at the cathode/O^{2–} conducting electrolyte interface [13],

they investigated H₂O reduction kinetic processes at Pt/YSZ interface [14], La_{0.8}Sr_{0.2}CrO₃/YSZ interface [15] and Pt–La_{0.8}Sr_{0.2}CrO₃/YSZ interface [16]. They also studied the kinetic evolution of H₂O reduction with current density [17].

It is also worth mentioning the work developed by Schouler on the relation between solid oxide electrolyte surface properties and electrode reaction kinetics, including the case of H₂O reduction [18] as well as Salzano et al. on process considerations in terms of engineering requirements to optimize energy efficiency of an SOEC system [19].

The HOTELLY project, through the studies reported by Döñiz et al., was of particular interest. Indeed, this project (which started in 1975) aimed at considering the industrial issues to integrate

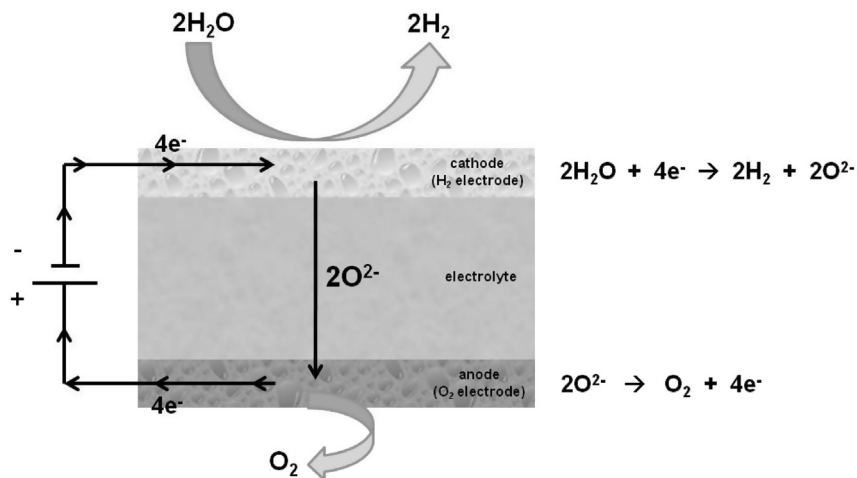


Fig. 1. Principle of high temperature steam electrolysis in the case of an oxide-ion conducting electrolyzer.

SOECs in a large scale electrolysis plant, leading to very promising results which showed the viability of such a way to produce hydrogen. Hence, in a first paper, Dönitz et al. presented first performance results with a cell voltage of 1.3 V for -0.4 A cm^{-2} applied, and first industrial engineering studies showing a total efficiency of 40–50% for the considered system [4]. Dönitz et al. then reported some results on the performance of tubular single cells and stacks, including a voltage of 1.15 V at -0.4 A cm^{-2} for the single cell and a stable voltage of about 1.2 V at -1 A during 800 h for the stack [20]. In another paper, a promising long-term test was performed on a single cell, with a constant cell voltage of 1.07 V at -0.3 A cm^{-2} for 1000 h, as well as a test on a tube composed of 10 cells connected in series showing a cell voltage of 1.33 V at -0.37 A cm^{-2} [21]. The latest performance result was reported in an additional paper where reversibility of the cells developed during this project was demonstrated with either hydrogen or carbon monoxide [22]. As part of the HOTELLY project, Quandt and Streicher discussed in detail a concept to build a 3.5 MW pilot plant [23].

Despite very promising technological perspectives shown by these first studies, hydrogen production by SOEC still implied important costs compared to other energy carriers such as fossil fuels. This surely explains, at least partly, the lack of interest for SOEC observed during most of the 1990s, as shown by the histogram (**Fig. 2**). However, key issues such as always growing energy needs, mid-term disappearance of important energy resources such as fossil fuels and global warming consecutive to massive greenhouse effect made production of renewable and clean energy essential. A possible answer can be the combination of solar photovoltaic, wind turbine and fuel cell, making hydrogen part of this energy mix as energy carrier. Hence, interest in SOEC has strongly grown since the end of the 1990s, as illustrated in **Fig. 2**, and particularly revealed by some very interesting performance studies [24–29]. However, cell degradation occurring during electrolysis is the technological limiting step to make SOEC meet performance targets economically viable for possible applications, especially those with long-term operations. This is the reason why more studies have been focusing on this topic during the last few years [30–35] (**Fig. 2**). Besides, the use of post-test characterization methods such as scanning electron microscopy (SEM), X-ray diffraction (XRD) or X-ray photoelectron spectroscopy (XPS) allows only limited understanding of degradation. Hence, using an *in-situ* method such as electrochemical impedance spectroscopy (EIS) can

be very helpful to get a better understanding of cell degradation mechanisms occurring during high temperature electrolysis, even if very few studies have been reported so far (**Fig. 2**). Thus, after a short presentation of EIS principle and data analysis methods followed by a brief SOEC materials state-of-the-art, this review will demonstrate how EIS can be used to (i) characterize electrode materials, both H₂ electrode and O₂ electrode; (ii) study cell degradation for different configurations: symmetrical cell, single cell and stack; (iii) develop a qualitative and quantitative systematic SOEC analysis approach with variation of parameters such as temperature, current density or $P_{\text{H}_2\text{O}}/P_{\text{H}_2}$ ratio.

2. EIS principle and data analysis methods

2.1. EIS principle

Oliver Heaviside was the first to introduce the concept of electrical impedance in the 1880s, followed a few years later by Kennelly and Steinmetz who developed it in terms of vector diagrams and complex numbers representation [36,37]. According to Barsoukov and MacDonald [38], in the 1920s, impedance analysis of real systems (i.e. distributed in space) was developed by Carter with

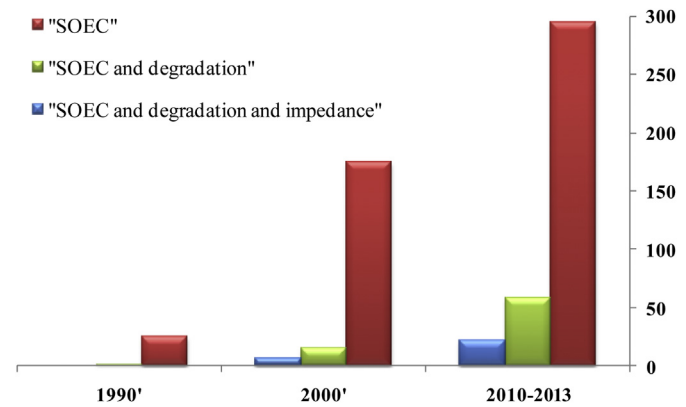


Fig. 2. Histogram representing the evolution of the number of publications according to Web of Science database from the 1990s to today (September 2013) for "SOEC" (red), "SOEC and degradation" (green), and "SOEC and degradation and impedance" (blue). (For interpretation of the references to colour in this figure legend, the reader is referred to the web version of this article.)

the circle diagram of electrical engineering [39] adapted to the study of dielectric systems in the 1940s by Cole and Cole with the plotting of ϵ' and ϵ'' in the complex plane now known as the Cole–Cole plot [40]. Later, from the 1940s, impedance has been extensively used in theoretical treatments of semiconductors and ionic systems including by Randles [41], Jaffé [42], Chang and Jaffé [43], Macdonald [44], and Friauf [45]. Since then, EIS has been developed to become a very strong experimental tool used in many fields of study, including the one discussed in this review.

According to Lvovich, similarly to resistance, impedance is the ratio between voltage and current, demonstrating the ability of a circuit to resist the flow of electrical current, represented by the “real impedance” term, but it also reflects the ability of a circuit to store electrical energy, like a capacitance, reflected in the “imaginary impedance” term. In other words, impedance can be defined as a complex resistance encountered when current flows through a circuit composed of various resistors, capacitors, and inductors, this definition being applied to both direct current (DC) and alternative current (AC) [37]. EIS is based on the measurement of a transfer function as a consequence of a disruption of the electrochemical system considered. When a disruption $a(t)$ is applied, a response $b(t)$ is emitted by the system, $a(t)$ and $b(t)$ being related by a transfer function $H(\omega)$ as follows:

$$B(\omega) = H(\omega) \cdot A(\omega)$$

with $A(\omega)$ and $B(\omega)$ the Fourier transforms of $a(t)$ and $b(t)$.

Since the applied disruption is usually sinusoidal, the applied signal is $a(t) = a_0 \sin(\omega t)$ and the emitted response is $b(t) = b_0 \sin(\omega t + \varphi)$ with a frequency f , a “radial frequency” $\omega = 2\pi f$, and a phase shift φ . Hence, electrochemical impedance is defined as the complex number $Z(\omega)$ with the expression

$$Z(\omega) = \Delta U(\omega) / \Delta I(\omega)$$

where, in potentiostatic mode, $\Delta U(\omega)$ is the applied disruption in voltage at a fixed potential U_0 ($\Delta U(\omega) = U_0 \sin(\omega t)$), and $\Delta I(\omega)$ the emitted response in current with a constant component I_0 ($\Delta I(\omega) = I_0 \sin(\omega t + \varphi)$). When measurements are done in galvanostatic mode, it is the current which is applied to the system and the voltage which is emitted as a response (see Fig. 3).

Using Euler's relationship ($\exp(j\varphi) = \cos\varphi + j\sin\varphi$, where j is defined as $j^2 = -1$), $Z(\omega)$ can be expressed as a combination of real (Z_R) and imaginary (Z_{IM}) parts as follows:

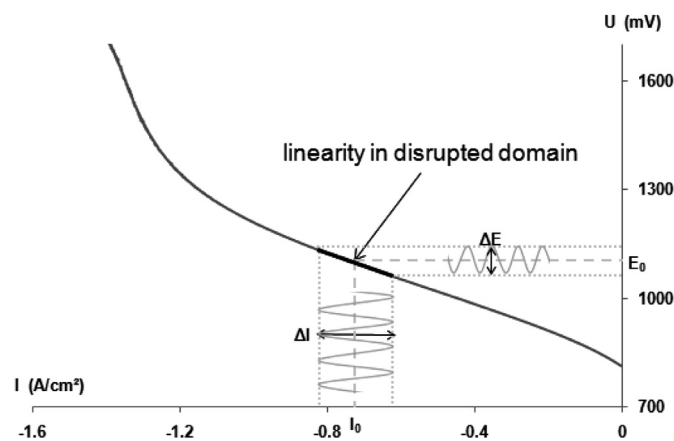


Fig. 3. Typical polarization curve with illustration of system disruption in galvanostatic mode.

$$Z(\omega) = |Z(\omega)| \exp(j\varphi) = |Z(\omega)| (\cos\varphi + j\sin\varphi) = Z_R + jZ_{IM}.$$

And the phase angle φ at a chosen ω

$$\tan\varphi = Z_{IM}/Z_R \text{ or } \varphi = \arctan(Z_{IM}/Z_R)$$

As expressed by Lvovich [37], Z_R and Z_{IM} can be respectively considered as an “in-phase” and an “out-of-phase” part of the impedance.

Since electrochemical systems considered are usually not stable with time and non-linear, measurements have to be done carefully. Indeed, one has to make sure that no evolution of the system occurs during the measurement, and the amplitude of the sinusoidal part of the applied signal has to be low enough to consider that the function $I = f(U)$ is linear in the disrupted domain (see illustration in Fig. 3).

Electrochemical impedance measurements are realized in a whole frequency range, typically from kHz to mHz, and usually represented in a Nyquist plot (Fig. 4a) or a Bode plot (Fig. 4b). By varying experimental parameters such as current applied, temperature, reactant composition, etc. frequency shifts in the impedance spectra can be observed, revealing information on electrochemical processes governing the system. Besides, one strong characteristic of this method is that measurements can be done while the system is functioning i.e. *in-situ* measurements, allowing access to information that would not be obtained otherwise (with post-mortem characterization methods for instance). However, the interpretation of impedance spectra can quickly become challenging, requiring the use of additional tools such as electrical equivalent circuit (EEC), distribution of relaxation time (DRT) or analysis of the difference in impedance spectra (ADIS) for a better and deeper understanding.

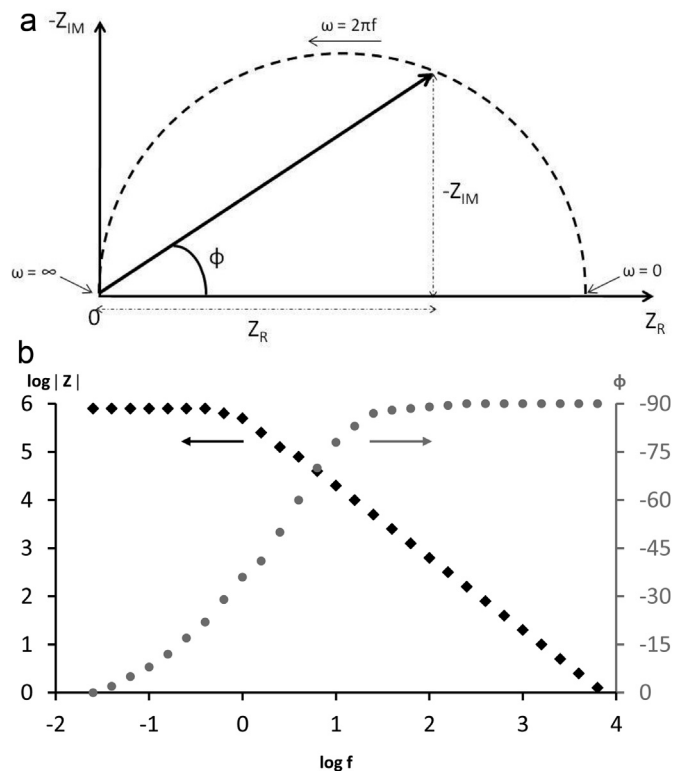


Fig. 4. Nyquist (a) and Bode (b) representation of complex impedance.

2.2. EIS data analysis methods

Here are briefly presented the most common methods used for EIS data analysis.

2.2.1. Electrical equivalent circuit (EEC)

Impedance diagram analysis is commonly performed using electrical equivalent circuits (EEC). This kind of analysis consists in fitting a measured impedance diagram with combination of ideal (resistor, capacitor, inductor, etc...) and non-ideal (constant phase element or CPE, Warburg, etc...) electrical elements in series and/or in parallel. Hence, the impedance diagram can be separated into different frequency ranges, each one represented by part of the EEC. This deconvolution of the impedance diagram allows distinguishing the main contributions governing the system considered, each contribution associated to a frequency range, a relaxation frequency and the electrical element values. Therefore, discussions based on variation laws deduced from impedance evolutions, their analysis through modeling and literature data lead to the identification of the main physical and electrochemical phenomena explaining both functioning and evolution of the system. Moreover, depending on the system considered, physico-chemical data such as kinetic parameters, diffusion coefficients or dielectric constants can be obtained. Two typical EECs used for SOEC are shown as examples in Fig. 5. The first EEC (Fig. 5a) is composed of a resistance in series with an inductance and in series with three circuits of a resistance in parallel with a constant phase element. In cases where a contribution related to gas diffusion process is particularly dominant, the second EEC (Fig. 5b), where a CPE is replaced by a Warburg element, can be more adapted. However, although the use of EECs seems to be “basic”, it must be done with the care of ensuring consistency between the trends showed by the measured impedance diagrams and the values of the electrical elements obtained with the fitting, since fitting of an impedance diagram based on a mathematical program will always lead to acquisition of values but not necessarily to any physical meaning. Furthermore, the main weakness of this approach is the need of an *a priori* defined EEC, which means that subjectivity of the user in the choice of this pre-defined EEC may influence the consequent analysis.

To briefly mention it, the constant phase element (CPE), widely used to fit impedance diagrams, is often used to describe a non-ideal capacitive behavior. The term “constant phase element” means that the phase angle of the portion of a circuit represented by this element is AC frequency independent [37]. The CPE impedance is expressed as:

$$Z_{\text{CPE}} = 1/Y_0(j\omega)^n$$

where $Y_0(s^n/\Omega)$ and n are the frequency independent CPE model parameters.

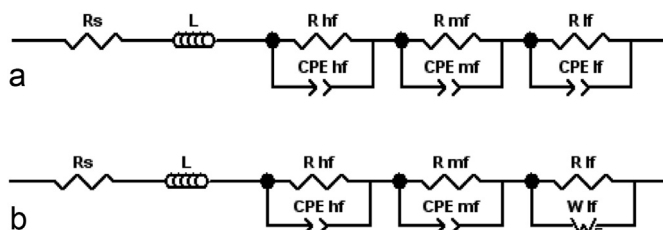


Fig. 5. Two typical EECs used for SOEC. The first EEC (a) is composed of a resistance in series with an inductance and in series with three circuits of a resistance in parallel with a constant phase element. In cases where a contribution related to gas diffusion process is particularly dominant, the second EEC (b), where a CPE is replaced by a Warburg element, can be more adapted.

Since impedance diagrams of SOEC systems are often fitted with circuits including a resistance in parallel with a CPE, one should notice that the Nyquist plot of a resistance in parallel with a CPE is a depressed semicircular arc with an angle of $(n - 1) \times 90^\circ$. Besides, depending on the n value, the CPE can describe several behaviors. For instance, when $n = 1$, the CPE corresponds to a pure capacitor with $Y_0 = C$ while when $n = 0$, the CPE represents an ideal resistor with $Y_0 = 1/R$. In addition, in the special case of $n = 0.5$, the CPE is assimilated to a Warburg element which represents the impedance created by the diffusion resistance to current flow carried by electroactive species [37]. Thus, according to Lvovich [37], depending on the n value and the system considered, the CPE can be associated to (i) electrode inhomogeneity and surface roughness; (ii) electrode porosity; (iii) variability in thickness and conductivity of surface coating; (iv) slow, uneven adsorption process; (v) nonuniform potential and current distribution at the surface; (vi) grain boundaries and crystal phases on polycrystalline electrode. However, one has to keep in mind that despite a good ability to fit impedance diagrams, interpretation of the CPE behavior and so its association to one of these processes can be particularly difficult. CPE and Warburg element are described and discussed in more details elsewhere [37].

2.2.2. Analysis of the difference in impedance spectra (ADIS)

According to Jensen et al. [46], analysis of the difference in impedance spectra (ADIS) is a method based on the change occurring in an impedance spectrum when an optional operation parameter such as partial pressure of a reactant, temperature, etc., is changed. An impedance spectrum is recorded just before such a change and another spectrum just after it. The real part of the spectra is differentiated with respect to $\ln(f)$, where f is the frequency. The difference in this quantity, $\partial Z'(f)/\partial \ln(f)$, between the two spectra is named $\Delta Z'$ and is plotted vs $\log(f)$. The resulting spectrum enables detection of processes affected by the altered operation parameter. The difference in the imaginary part of the two impedance spectra (named $\Delta Z''$) contains almost the same information. However, plotting $\Delta Z''$ vs $\log(f)$ does not provide the same resolution in the frequency domain. In addition, the $\Delta Z'$ spectrum may provide detailed information about the nature of the involved processes. Thus, the ADIS approach allows analyzing the variations of a measured impedance diagram as a consequence of the variation of a parameter. A complete study may finally lead to the identification of one or several phenomena related to the system considered. However, the quantification in term of relative importance of a phenomenon compared to the others requires the use of an EEC. ADIS theory is explained in more details elsewhere [46,47].

2.2.3. Distribution of relaxation time (DRT)

According to Schichlein et al. [48], a direct access to the dynamic constants in the impedance data is provided by the relaxation times (rate constants) and relaxation amplitudes (loss factors) of the impedance-related processes. In impedance data analysis, the distribution of relaxation times is the basic quantity of interest. However, the relaxation times cannot be measured directly, because an impedance measurement at a given radial frequency ω contains significant contributions from any relaxation time above and below ω^{-1} . For systems with relaxation processes separated by at least two decades in frequency, such a poor ‘resolution’ is totally adequate [49]. However, in complex electrochemical situations, such as practical solid oxide cells operation, the contributions of physically distinct processes merge and a meaningful interpretation of the results is difficult. DRT is a deconvolution method that allows the direct calculation of a distribution function of relaxation times and relaxation

amplitudes of impedance-related processes directly from experimental data. Moreover, distributions of relaxation times provide a direct access to the kinetic parameters of the underlying processes. In order to obtain these distributions, no *a priori* choice of an equivalent electrical circuit model with subsequent non-linear least squares curve fit is required. Fourier analysis of the impedance spectra, in combination with extrapolation techniques and digital filtering in the transformed space of the data has to be applied to achieve such results. The DRT approach is particularly interesting because it allows preventing any user subjectivity. Thus, DRT analysis of an impedance diagram can be used as a pre-identification tool to select the EEC most adapted to the studied system. Consequently, the combined use of DRT and EEC is strongly recommended to optimize an objective EIS analysis. Moreover, whatever the electrochemical configuration (two or three electrodes), DRT analysis should enable discerning the different impedance contributions. In the case of SOECs, and particularly for cells including thin electrolytes, this approach can lead to the separation of anodic and cathodic contributions without the use of a reference electrode. DRT theory is explained in more details elsewhere [48,50].

3. Electrode performance and mechanisms characterization by EIS

3.1. Typical SOEC electrodes

Before presenting more specifically SOEC electrodes, electrolyte material must be briefly mentioned. Yttria-stabilized zirconia (YSZ) is by far the most widely used material as electrolyte of solid oxide cells (SOCs) and remains a reference, even if materials such as $\text{La}_{0.9}\text{Sr}_{0.1}\text{Ga}_{0.8}\text{Mg}_{0.2}\text{O}_3$ (LSGM) [51,52] or one particular composition of scandia-doped zirconia, i.e. the 1 mol% CeO_2 10 mol% Sc_2O_3 stabilized ZrO_2 (1Ce10ScSZ) [83,84], are considered in some studies.

3.1.1. Anodic material (O_2 electrode)

Srontium-doped lanthanum manganite (LSM)–YSZ composite has been extensively used as oxygen electrode material for both SOFCs and SOECs due to its good electronic conductivity, good catalytic properties at elevated operating temperatures, excellent long-term stability and a thermal expansion behavior close to the typical YSZ electrolyte [53–55]. It is however difficult to obtain a uniform LSM–YSZ composition which would increase the length of the triple phase boundary (TPB) region LSM/YSZ/gas. Sr-doped LaCoO_3 (LSCO) and Sr-doped LaFeO_3 (LSF) seem to be interesting since they showed much lower polarization losses than electrodes based on LSM in SOFC mode [56–58]. Another possible alternative is to consider the mixed ionic-electronic conducting electrodes such as promising lanthanum strontium cobalt ferrite (LSCF). Indeed, in addition to a high electronic conductivity, LSCF electrode exhibits high oxygen ion conductivity [58–60] which is expected to result in an enlargement of the area where oxygen reaction can take place [61,62] and to high oxygen surface exchange coefficients for faster kinetics at the gas/electrode interface [63]. $\text{Ln}_2\text{NiO}_4 + \delta$ -type oxides (with the K_2NiF_4 -type structure) are also interesting because of their aptitude to accommodate a large oxygen overstoichiometry, especially under oxidizing conditions [64], this capability leading to a mixed electronic and ionic conductivity. $\text{Nd}_2\text{NiO}_4 + \delta$ oxide is especially studied because of its higher overstoichiometry compared to the other $\text{Ln}_2\text{NiO}_4 + \delta$ -type oxides [65], which leads to further improved performances [66,67]. It is also worth mentioning $\text{BaCo}_{0.7}\text{Fe}_{0.2}\text{Nb}_{0.1}\text{O}_3 - \delta$ (BCFN) oxide [52] and $\text{Sr}_2\text{Fe}_{1.5}\text{Mo}_{0.5}\text{O}_6 - \delta$ (SFM) perovskite [51], both recently studied as potential SOEC anode materials.

3.1.2. Cathodic material (H_2 electrode)

Nickel–yttria-stabilized zirconia (Ni–YSZ) is the most common material used as hydrogen electrode for both SOEC and SOFC configurations thanks to its excellent electrocatalytic properties notably due to a porous cermet (ceramic–metal composite) structure which provides percolation paths for electrons, oxygen ions and gas, as well as a thermal expansion coefficient close to the typical YSZ electrolyte [67,68]. Nickel–scandia-stabilized zirconia (Ni–ScSZ) is an alternative choice for Ni–YSZ which is gaining attention [69], especially for applications at intermediate temperature since it shows better ionic conductivity [70,71]. Perovskite strontium-doped lanthanum chromo-manganite $(\text{La},\text{Sr})(\text{Cr},\text{Mn})\text{O}_3$ (LSCM), which is electrochemically active and redox stable as SOFC anode material [72–74], also seems to be a good candidate as an SOEC cathode material according to the several studies recently reported [75–78]. SFM mentioned before was also studied as potential SOEC cathode material [51].

3.2. O_2 electrode characterization

Table 1 contains the main characteristics of the cells studied in the papers discussed below in terms of cell configuration and composition, EIS measurement conditions as well as measured resistances.

EIS can be used to characterize the electrode material performance and the electrode/electrolyte interface. In such cases, the discussion is based on the variation of the ohmic resistance (R_s), related to the resistance of the electrolyte and the current collectors, and the polarization resistance (R_p), associated to the electrochemical processes. As mentioned before (see Section 3.1.1), LSM is widely used as anode for SOEC. The following papers focus on the influence of LSM microstructure on its electrochemical performance. Bernuy et al. studied the effect of LSM porosity, sintering temperature and LSM impregnation on the electrochemical performance [79]. The comparison of R_s and R_p showed that the best oxygen electrode is the one with 20% of porosity, sintered at 1210 °C and impregnated with nano-sized LSM. This sample is dominated by a low frequency arc thermally activated with a characteristic frequency of 5 Hz. However, the formation of $\text{La}_2\text{Zr}_2\text{O}_7$ at the LSM/YSZ interface, characterized by an important increase in R_s , decreased dramatically the performance of the cell and a way to avoid its formation is hence needed. Yang et al. fabricated a strontium-doped LSM–YSZ oxygen electrode (0.35 cm² active area) with a porous network-like microstructure and characterized its effect on the performance of the electrolysis [80]. They first showed that R_s is independent of current density and decreases when temperature increases, while R_p decreases when both current density and temperature increase, as already observed elsewhere [92,104,124,128]. Besides, R_p values obtained in this study are lower than what reported elsewhere [81,82]. The additional use of SEM and XRD allowed suggesting that these better performances are due to the fact that the LSM/YSZ/gas three phase boundaries are greatly extended in the porous network-like LSM–YSZ oxygen electrode. It would be interesting to see if this beneficial effect is still valid in a cell with bigger dimension. Liang et al. prepared a highly homogenous LSM–YSZ composite powder using an *in-situ* glycine–nitrate combustion method for SOEC [82]. Based on the electrochemical test results, the mechanism showed in Fig. 6 was proposed for the activation process of O^{2-} oxidation on LSM–YSZ electrodes, which involved the incorporation of surface segregated SrO into the LSM lattice and generation of oxygen vacancies in the LSM–YSZ electrodes. It would be useful though to know how this material would behave when typical parameters (i, T, etc...) are varied.

Table 1

Main characteristics of the cells studied in the papers reported Section 3.2 in terms of cell configuration and composition, EIS measurement conditions as well as measured resistances.

Ref.	Cell configuration	O ₂ electrode	Electrolyte	H ₂ electrode	Active area (cm ²)	Frequency range Signal amplitude Fitting with EEC	Parameters studied using EIS	Experimental conditions to measure R _s and R _p	R _s (Ω cm ²)	R _p (Ω cm ²)
									R _{HF}	R _{MF}
[79]	Symmetrical cell	LSM–YSZ (support)	Sc–YSZ	LSM–YSZ	—	82,540–0.08 Hz — No	Porosity, sintering temperature, LSM impregnation	850 °C OCV Air	0.09	0.24
[80]	Complete cell	LSM–YSZ	YSZ	Ni–YSZ (support)	0.33 cm ²	10 kHz–n.c. — No	i (0, 0.1, 0.3, 0.5, 0.7 A cm ⁻²) T (800, 900 °C)	800 °C 0.7 A cm ⁻² Air 50% H ₂ O	0.45	0.79
[82]	Complete cell	LSM–YSZ	YSZ	Ni–YSZ (support)	0.9 cm ²	100 kHz–0.5 Hz 10 mV No	Time (0, 3, 17, 22 min)	900 °C OCV Air 60% H ₂ O t = 22 min	0.4	0.71
[83]	Complete cell	LSCF LSM–YSZ	10Sc1CeSZ (support)	Ni–YSZ	—	10 kHz–0.1 Hz 50 mV Yes	Oxygen electrode	800 °C OCV Air 70% H ₂ O	0.152 0.159	0.078 0.067 0.582 0.776
[84]	Complete cell	LSCF LSM–YSZ	10Sc1CeSZ (support)	Ni–YSZ	—	10 kHz–0.1 Hz 20 mV No	T	800 °C OCV Air 70% H ₂ O	0.15 0.15	0.51 0.81
[85]	Complete cell	LSM–YSZ BSCF	YSZ	Ni–YSZ (support)	0.785 cm ²	10 kHz–0.1 Hz 20 mV No	Time (0, 20 h)	800 °C OCV Air 50% H ₂ O	— 0.22	— 0.5
[86]	Complete cell	LSF–YSZ LSCo–YSZ LSM–YSZ	YSZ	Co-ceria–YSZ (support)	0.35 cm ²	100 kHz–0.01 Hz 5 mV No	i (0.03, 0.145 mA cm ⁻²)	700 °C 0.140 A cm ⁻² Oxygen 15% H ₂ O	0.65 0.55 0.65	0.35 0.2 0.65
[66]	Complete cell with Au reference	Nd ₂ NiO _{4+δ}	YSZ (support)	Ni–CGO	3.14 cm ²	10 ⁴ –10 ⁻¹ Hz 100 mA No	T (750, 800, 850 °C)	750 °C OCV Air 90% H ₂ O Ar for reference	0.72 (cathode) 0.07 (anode)	0.1 (cathode) 0.35 (anode)
[67]	Symmetrical or half cell with Pt reference	LSM La ₂ NiO _{4+δ} Nd ₂ NiO _{4+δ} Pr ₂ NiO _{4+δ}	YSZ (support)	LSM La ₂ NiO _{4+δ} Nd ₂ NiO _{4+δ} Pr ₂ NiO _{4+δ}	0.8 cm ²	10 ⁶ –10 ⁻² Hz 100 mV No	T (600, 650, 700, 750, 800, 850 °C)	T ∈ [600, 900 °C] OCV Air	— — — —	~10 ~1 ~1 ~1
[51]	Symmetrical cell	SFM	LSGM (support)	SFM	0.33 cm ²	100 kHz–0.01 Hz — No	T (800, 850, 900 °C) % H ₂ O (20, 40, 60%) i (0, 0.1, 0.3, 0.5, 0.7 A cm ⁻²)	800 °C OCV Air 60% H ₂ O	0.54	0.83
[52]	Symmetrical (BCFN) and complete cell	BCFN	LSGM (support)	Ni–CGO	0.33 cm ²	100 kHz–0.1 Hz 10 mV No	O ₂ partial pressure (0.2, 0.8), T (750, 800, 850 °C) % H ₂ O (20, 40, 60%)	800 °C OCV Air 60% H ₂ O	0.27	0.05

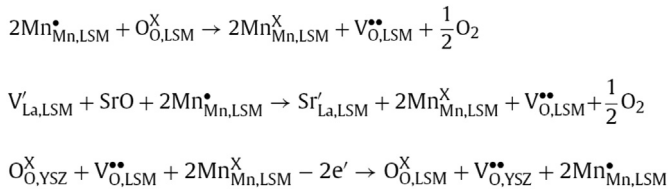


Fig. 6. Mechanism proposed by Liang et al. for the activation process of the O²⁻ oxidation on LSM–YSZ electrodes [82]. Elsevier permission.

The following studies show how EIS is also used to compare the behavior of several possible anode materials, with LSM taken as reference material. In a first paper, Laguna-Bercero et al. reported their analysis on electrochemical cells after combined SOFC–SOEC tests, in terms of structural, microstructural and electrical characterization for both LSM–YSZ and LSCF perovskite-based electrodes [83]. The cell was supported by a scandia-stabilized zirconia substituted with a ceria electrolyte (10Sc1CeSZ). R_p values were found to decrease according to the following order: Pt > LSM12 > LSM10 > LSCF, while a 10% increase in the R_s value of the LSM sample was observed. It seems to be consistent with a distortion of the rhombohedral $\beta\text{-Sc}_2\text{Zr}_7\text{O}_{17}$ phase observed by XRD. In addition, the impedance response at OCV, analyzed using an EEC, included a large arc at low frequencies (relaxation frequency at about 200 Hz) associated with the oxygen electrode. In a second paper, Laguna-Bercero et al. compared again LSM–YSZ and LSCF electrodes [84]. In this case again, R_p was higher for LSM than for LSCF. Nevertheless, at 800 °C, whatever the electrodes the cell was almost reversible and could work in SOFC or SOEC mode. Even if both LSCF and LSM–YSZ using scandia–zirconia-based cells present encouraging results, further studies are required to characterize their long-term stability. Kim et al. compared the performance of SOECs made from LSM–YSZ and BSCF ($\text{Ba}_{0.5}\text{Sr}_{0.5}\text{Co}_{0.8}\text{Fe}_{0.2}\text{O}_{3-\delta}$) oxygen electrodes [85]. BSCF cell showed better performance than LSM–YSZ cell. However, significant performance decay of the BSCF cell was observed under electrolysis mode compared to a relatively stable LSM–YSZ cell performance under the same operating conditions. This was characterized by an increase in both R_s and R_p for the BSCF cell. Wang et al. prepared and tested LSM, LSF and LSCo oxygen electrodes [86]. Similar R_s values were obtained for all three cells. Meanwhile, LSF and LSCo showed better performance than LSM characterized by lower R_p values. LSF and LSCo exhibited impedances that seem to be only slightly dependent on current density. Further measurements are however needed to confirm these trends for higher applied current densities.

The following papers deal with promising nickelate-type and perovskite-type anode materials recently studied. Nickelate-type material $\text{Nd}_2\text{NiO}_4 + \delta$ was investigated by Chauveau et al. [66]. The EIS study of the influence of temperature on the behavior of this material showed that R_p decreases with increasing temperature, indicating that electrochemical processes are thermally activated for both electrodes. However, the diagrams and their frequency distribution were similar, showing that the electrochemical processes remain unchanged for the considered temperature range. Thanks to the use of a specific set-up containing a reference electrode, anodic and cathodic contributions were separated, showing that R_p is higher for the O₂ electrode. Moreover, Ogier et al. [67] compared three nickelate-type materials ($\text{La}_2\text{NiO}_4 + \delta$, $\text{Nd}_2\text{NiO}_4 + \delta$, $\text{Pr}_2\text{NiO}_4 + \delta$) to LSM and observed that R_p values were more than 10 times lowered for the nickelates, characterized by better performances. These results were obtained with a single atmosphere half cell set-up. It would thus be interesting to study the behavior of these materials with a single cell set-up. Liu et al. prepared and tested a perovskite-type material, $\text{Sr}_2\text{Fe}_{1.5}\text{Mo}_{0.5}\text{O}_6 - \delta$

(SFM) in a dual atmosphere symmetrical cell configuration using $\text{La}_{0.8}\text{Sr}_{0.2}\text{Ga}_{0.83}\text{Mg}_{0.17}\text{O}_{3-\delta}$ (LSGM) as electrolyte [51]. By comparing their study with that of Yang et al. presented earlier [80], they noticed that the R_p values of the SFM/LSGM/SFM symmetrical cell were smaller than the values reported by Yang et al. for a LSM–YSZ/YSZ/Ni–YSZ cell in similar operation conditions. In addition, the cell showed a relatively good stability during a 100 h test. In another paper, Yang et al. recently fabricated and characterized a novel perovskite-type material, $\text{Ba}_{0.9}\text{Co}_{0.5}\text{Fe}_{0.4}\text{Nb}_{0.1}\text{O}_{3-\delta}$ (BCFN) as a potential SOEC oxygen electrode using LSGM as electrolyte [52]. This material showed usual trends with temperature and oxygen partial pressure change: their increase leads to R_p decrease. Moreover, the cell was stable during a 200 h test. Thus, SFM and BCFN seem to be very promising electrode materials for SOECs based on LSGM electrolyte. However, it would be interesting to investigate them with the standard electrolyte material YSZ to have a wider comparison range.

3.3. H₂ electrode characterization

Table 2 shows the main characteristics of the different cells mentioned in this part in terms of cell configuration and composition, EIS measurement conditions as well as measured resistances.

As mentioned before (see Section 3.1.2), Ni–YSZ cermet is by far the most widely used cathode material in a SOEC. Therefore, in most of SOEC studies, including the ones discussed in this review, Ni–YSZ is the material used as H₂ electrode. Two interesting papers on EIS performance and behavior characterization of Ni-based cermet cathode are worth mentioning. In the first one, Liang et al. prepared a nano-sized NiO powder on submicron-sized YSZ particles via an *in-situ* coating method [87]. Several composite powders were prepared with different $\text{CO}(\text{NH}_2)_2/\text{Ni}(\text{NO}_3)_2$ ratios and each one was used as cathode of the single cell Ni–YSZ/YSZ/LSM–YSZ. An EIS analysis of each single cell was performed using an EEC composed of R_s for the ohmic resistance of the cell and current collectors, L for the inductance of the current collectors, R_{HF}/CPE_{HF} for the high frequency arc and R_{MF}/CPE_{MF} for the middle frequency arc. The very interesting point is that for each analyzed cell, R_s and R_{HF} were similar ($\sim 0.2 \Omega \text{ cm}^2$) while R_{MF} was much higher ($\sim 1 \Omega \text{ cm}^2$). Thus, the performance difference between the cells was caused by Ni–YSZ electrodes. This suggests that H₂O adsorption and diffusion of the Ni–YSZ electrode is the limiting step in the whole electrolysis reaction. However, it would have been more valuable to mention and discuss the capacitance values obtained from CPE parameters' values in order to confirm or deny the above suggestion. In the second paper, Patro et al. fabricated a symmetrical cell composed of YSZ and the novel Ni–1Ce10ScSZ cermet cathode presented before (see Section 3.1.2) [69]. The influence of the following parameters on the symmetrical cell polarization resistance was determined using EIS: sintering temperature, NiO percentage in Ni–1Ce10ScSZ, thickness of coating, number of current collecting layers and number of YDC layers between the electrolyte and the electrode. A temperature of 1300 °C was found to be the most optimized sintering temperature and the 60% NiO–40% ScSZ (vol. %) as the most suitable composition. Besides, the coating thickness of 35 nm corresponding to 5 layers of coating gave the minimum R_p value. Moreover, it was found that there is no noticeable effect of applying a current carrying layer with such a functional layer and a negative effect resulted when YDC interface layer was applied to it. The next step of this very useful investigation would be to test this optimized Ni–1Ce10ScSZ as cathode in a single cell configuration.

Other investigations were made on one of the possible alternative cathode material, the strontium-doped lanthanum

Table 2

Main characteristics of the different cells mentioned in Section 3.3 in terms of cell configuration and composition, EIS measurement conditions as well as measured resistances.

Ref.	Cell configuration	O ₂ electrode	Electrolyte	H ₂ electrode	Active area (cm ²)	Frequency range Amplitude signal Fitting with EEC	Parameters studied using EIS	Experimental conditions to measure R _s and R _p	R _s (Ω cm ²)	R _p (Ω cm ²)	
									R _{HF}	R _{MF}	
[87]	Complete cell	LSM–YSZ	YSZ	Ni–YSZ (support)	0.9 cm ²	100 kHz–0.5 Hz 10 mV Yes	Composition of NiO–YSZ composite powder	900 °C OCV Air 80% H ₂ O	~0.1	~0.2	~1
[69]	Symmetrical cell	Ni–1Ce10ScSZ	YSZ (support)	Ni–1Ce10ScSZ	–	10 ⁶ –10 ⁻¹ Hz – No	Sintering temperature NiO % in Ni –1Ce10ScSZ Thickness of coating nb of collecting layers nb of YDC layers	800 °C 3% H ₂ O	– 0.17 (60% NiO) – – – –	0.97 (1300 °C) 0.86 (60% NiO) 0.95 (5 layers) ~0.95 ~1	
[78]	Symmetrical cell	LSCM–YSZ	YSZ (support)	LSCM–YSZ	0.785 cm ²	10 ⁵ –10 ⁻² Hz 50 mV No	P _{H₂O} /P _{H₂} = 1, 2 or 5	850 °C OCV	1.3	2.1	
[77]	Complete cell	LSM	YSZ (support)	LSCM–YSZ	0.5 cm ²	100 kHz–0.1 Hz 10 mV No	i (0, 40, 80, 120 mA cm ⁻²) T (800, 850, 900 °C) % H ₂ O (20, 40, 60, 80%)	800 °C OCV O ₂ 60% H ₂ O	0.86	1.5	
[66]	Complete cell with Au reference	Nd ₂ NiO _{4 + δ}	YSZ (support)	Ni–CGO	3.14 cm ²	10 ⁴ –10 ⁻¹ Hz 100 mA No	T (750, 800, 850 °C)	750 °C OCV Air 90% H ₂ O Ar for reference	0.72 (cathode) 0.07 (anode)	0.1 (cathode) 0.35 (anode)	

chromo-manganites $(\text{La},\text{Sr})(\text{Cr},\text{Mn})\text{O}_3$ (LSCM). Ringuedé et al. characterized different electrode architectures based on composite LSCM/YSZ material [78]. The EIS measurements on the symmetrical cell showed that steam content has little influence on the material behavior as cathode. Among all the studied assemblies, the optimal architecture was composed of a 10 μm functional layer of at least 60 wt% LSCM and of a 30 μm pure LSCM collecting layer. However, regarding the whole study including i – U measurements, an additional collecting layer seems to be necessary with LSCM as cathode of a SOEC. In another paper, Jin et al. worked on a SOEC based on LSCM hydrogen electrode [77]. Various current densities, temperatures and steam partial pressures were used to understand the cell behavior. As usually observed for Ni–YSZ [92,104,124,128], increasing current density or temperature leads to a decrease in R_p . More interesting to notice in this case is the influence of steam partial pressure. Indeed, contrarily to what is widely reported for Ni–YSZ [104,120,121,124,128], R_p increases with increasing steam partial pressure. This could be due to a smaller porosity of LSCM compared to Ni–YSZ. The porosity of LSCM was not specified by the authors to confirm this possible explanation. The same behavior was observed for SFM, a material mentioned before (see Section 3.1) which was also studied as potential cathode material. This behavior at higher steam partial pressure should be improved for these two materials to become serious alternatives as cathode material of a SOEC.

Another material was recently used as SOEC cathode, Ni–CGO cermet [66]. However, even if Chauveau et al. measured an impedance diagram of Ni–CGO thanks to a configuration containing a reference electrode, no EIS analysis focusing on the behavior of this material has been done so far.

4. SOEC degradation study by EIS

As discussed previously, EIS can be very useful to characterize the performance and the behavior of electrode materials. The following part is focused on studies where EIS has a use in the understanding of cell degradation for different configurations considered: symmetrical cell, single cell and stack.

Table 3 summarizes the main experimental conditions for the papers reported in this part.

4.1. Symmetrical cell

In this paragraph, the authors focused on cells including two identical electrodes in the same atmosphere. Keane et al. investigated the LSM anode delamination behavior by applying voltages ranging from 0 V to 0.8 V with respect to OCV [88]. They observed the development of a weak anode/electrolyte interface with the applied voltage leading to the delamination of the anode, characterized by an important increase in both R_s and R_p . It would certainly be interesting to further analyze the possible frequency shifts in the impedance diagrams measured and relate them to the post-test observations. In the second paper considered, Chen and Jiang studied in detail the delamination behavior of LSM as oxygen electrode of an SOEC under an anodic current passage of 500 mA cm^{-2} for 48 h [89]. In this case as well, the delamination occurred at the electrode/electrolyte interface through the formation of nanoparticles (cf. illustration Fig. 7) and was also characterized by a significant increase in both R_s and R_p . The use of an EEC allowed separating the impedance diagrams into two arcs and so R_p into two terms: a high frequency arc (HF arc) characterized by R_{HF} and suggested to be related to the oxygen ion migration from the LSM electrode to the YSZ electrolyte, and a low frequency arc (LF arc) characterized by R_{LF} and suggested to be related to the oxygen dissociation and surface diffusion. By separating R_p into R_{HF} and R_{LF} ,

Chen and Jiang could observe an important increase in R_{HF} with the appearance of delamination while no significant variation on R_{LF} was noticed, indicating that (i) the electrode process associated to the HF arc is closely related to the electrode/electrolyte interface, which strengthens its association to oxygen ion migration from the electrolyte to the LSM O_2 electrode; (ii) the electrode steps associated to the LF arc are not related to the oxygen migration and/or charge transfer at the electrode/electrolyte interface, which denies its association to oxygen dissociation and surface diffusion [90,91]. Chen et al. confirmed these trends in a second study where the same cell was tested for 100 h [92]. They first observed once again the influence of the degradation at the electrode/electrolyte interface on R_{HF} mainly. But more interesting, they calculated activation energies that strengthen the conclusion from their first study mentioned above. Indeed, they calculated an activation energy of 83 kJ mol^{-1} (0.86 eV) for R_{HF} which is close to the activation energy value of 100 kJ mol^{-1} (1.04 eV) associated to the oxygen reduction reaction electrode process occurring at high frequency [93] and an activation energy of 125 kJ mol^{-1} (1.30 eV) for R_{LF} which is significantly lower than 170–202 kJ mol^{-1} (1.76–2.09 eV) corresponding to the low frequency electrode process associated with the oxygen dissociation and surface diffusion on the LSM electrodes [93–95]. A possible way to clearly identify the phenomena related to the LF arc would be to carry out other degradation tests with the change of one parameter per test such as anodic current, gas composition or gas distribution, and to analyze their influence on the LF arc. In the last paper mentioned in this paragraph, Chen et al. studied the electrochemical performance and stability of a palladium-infiltrated LSM–GDC composite SOEC anode under current applied for 100 h [96]. They first showed that adding GDC to LSM leads to a significant increase in the TPB areas for the oxygen oxidation reaction characterized by an important decrease in R_p . However, the LSM–GDC composite showed a poor stability when current was applied. They also observed that Pd nanoparticles infiltration leads to (i) a significant enhancement of the electrocatalytic activity of LSM–GDC characterized, here as well, by an important decrease in R_p , and more particularly R_{LF} ; (ii) a much more stable behavior of LSM–GDC during the 100 h test, even if degradation of this composite material finally occurred with the agglomeration of Pd nanoparticles. This degradation could be prevented by inhibiting this agglomeration, possibly by alloying Pd with Mn or Co [97,98].

4.2. Single cell

The first papers considered discuss the possible degradation of the cell by impurities. The term “passivation” used in this paragraph refers to a reversible degradation of the cell. In a first study, Hauch et al. tested several locally produced SOFCs in HTE mode for up to 766 h [99]. The cells were passivating, mainly during the first 100 h of electrolysis, and could be partly activated again by running an i – U curve in fuel cell mode or working in constant electrolysis conditions (Fig. 8). In terms of EIS, passivation and activation of the cell were respectively characterized by an increase and a decrease in R_p (Fig. 8), while R_s remained constant during the entire test. More interesting is that impedance diagrams recorded during passivation and activation at constant conditions were found to overlap for each frequency, which strongly suggests that the rate limiting steps during both passivation and activation are associated to the same processes (Fig. 9). Furthermore, passivation was characterized by a shift of the HF part of the impedance diagram associated to charge transfer at the electrode/electrolyte interface, as presented before. Hence, based on the observation of impurities containing silica and on the work done by Jensen et al. [46], Hauch et al. suggest that (i) passivation of the cell might be due to a

build-up of glassy phase impurities at the TPB of the H₂ electrode leading to an increase in the diffusion path length at the TPB and (ii) its partial activation could be explained by a break-up of the glass, consequently to the crystallization of these glass phases, which would lead to a decrease in the diffusion path length at the TPB and enable the observed complete overlap of the impedance diagrams during passivation and activation. Another study made by Hauch et al. strengthens these suggestions [100]. Indeed, SOE cells tested for 1000 h were found to passivate because of silica impurities segregation to the Ni–YSZ/YSZ interface (cf. illustration Fig. 10) characterized by R_s and/or R_p increase, depending on test conditions. Silica impurities observed by SEM are supposed to segregate from glass sealing. In an additional study [101], Hauch et al. verified that silica impurities segregate from the applied glass sealing to the H₂ electrode/electrolyte interface by changing the sealing. Besides, based on a cell degradation study by EIS and the use of the deconvolution model by Barfod et al. [102], they showed that degradation of the cell was characterized by an increase in the resistance at higher frequency part of the impedance diagram assigned here to charge transfer at the H₂ electrode [103]. In the next study, Ebbesen et al. examined for more than 1300 h degradation of a cell similar to the one discussed just before [99–101] in both H₂O electrolysis and co-electrolysis of H₂O and CO₂ [47]. In this case, impurities originated from inlet gases. Indeed, when inlet gases were applied as received, degradation of the cell occurred with an initial passivation of the cell followed by a long-term degradation. This degradation was characterized by an increase in R_p . The use of ADIS allowed identifying two contributions to this degradation: one at the Ni–YSZ electrode characterized by a relaxation frequency of 100–200 Hz and one occurring either at the Ni–YSZ or LSM–YSZ electrodes characterized by a relaxation frequency of 1000–3000 Hz. Cleaning the inlet gases leads to the disappearance of the former contribution, meaning that this contribution is surely caused by adsorption of impurities at the Ni–YSZ/YSZ interface, similar to what mentioned above [99–101]. Graves et al. also studied the same kind of cell for up to 382 h in co-electrolysis [104]. By analyzing the DRTs of the impedance diagrams measured, they distinguished two different degradation behaviors. When -0.25 A cm^{-2} is applied, degradation mainly occurs at the Ni–YSZ electrode whereas when -0.5 A cm^{-2} or more is applied, even if the Ni–YSZ electrode still degrades, R_s and degradation at the LSM/YSZ electrode contribute more significantly in the total loss of performance.

Studies discussed so far in this part focus on relatively low current densities applied (no more than -1 A cm^{-2}) which restrict possible degradation origins, simplifying the studied system. Nevertheless, it remains interesting to consider degradation for higher applied current densities, as shown by the two following studies. In the first one, Knibbe et al. examined the behavior of cells under high current densities (-1 , -1.5 and -2 A cm^{-2}) for up to 900 h [105]. Important degradation of the cell was observed, characterized by an important increase in R_s , while increase in R_p was not systematic. The observed R_s increase was attributed to oxygen formation in YSZ grain boundaries close to the LSM–YSZ/YSZ interface, based on the observation by TEM and SEM of increased porosity and fractures in these YSZ grain boundaries. In the second one, Sun et al. studied the co-electrolysis of H₂O and CO₂ on several cells, applying -1 and -1.5 A cm^{-2} for up to 932 h [106]. Degradation of the cells was observed, and results from impedance measurements indicated that the initial degradation (first 100 h) was mainly due to an increase in R_p while the long-term degradation (above 100 h) was, as for Knibbe et al., caused to a large extend by an increase in R_s , indicating structural changes of the electrodes. Thus, based on the ADIS analysis of the measured impedance diagrams, the gas shift study by EIS, and conclusions

from other studies made in SOFC mode [102,107–110], cell degradation at -1 A cm^{-2} was associated to the LSM–YSZ electrode, while both Ni–YSZ and LSM–YSZ electrodes were considered to contribute to cell degradation at -1.5 A cm^{-2} .

The next three papers report very interesting investigations dealing with particularly long-term degradation. In a first paper, Schefold et al. considered a LSM–YSZ/YSZ/Ni–YSZ commercial cell, applying -0.5 A cm^{-2} for up to about 1000 h [111]. The main change with time in impedance was the increase in the two contributions at intermediate frequencies between 3 kHz and 3 Hz, meaning that at least two processes are responsible for cell degradation in this case. One possible process might be the interfacial charge transfer, which typically appears in this frequency range [50,120–122,124,128]. Furthermore, a strong dependence of impedance diagram to $P_{\text{H}_2\text{O}}/P_{\text{H}_2}$ in this frequency range was observed, which surely means that an important part of cell degradation stems from the Ni–YSZ electrode, in accordance with what was observed elsewhere for different test durations [47,50,104]. The second paper from Schefold et al. is particularly interesting because of the test duration [112]. Indeed, the cell considered in this study (LSCF/YSZ/Ni–YSZ) was tested by applying -1 A cm^{-2} for 9000 h, which is the longest SOEC test reported so far, and with a comparatively low degradation rate of 3.8% (40 mV)/1000 h. In this case, impedance increase in the contribution from 10 kHz to 300 Hz was observed with time, here as well possibly associated to interfacial charge transfer [46,50,113,124,128]. Moreover, reactivation of the H₂ electrode was observed after 7615 h, characterized by an impedance increase in the same contribution. Both observations support a possible H₂ electrode deactivation with time. Furthermore, increase in a small contribution with a phase peak at 30 Hz was observed, attributed by the authors to mass transport at the H₂ electrode. Nevertheless, impedance diagrams showed that important part of cell degradation was due to the ohmic contribution since important increase in R_s was observed with time. This study was completed by Tietz et al. with a post-test analysis of the cell by SEM and EDX [114]. Hence, cell degradation was mainly characterized by (i) internal pore formation in YSZ electrolyte (Fig. 11) due to cation migration; (ii) compositional inhomogeneities and cation demixing in the LSCF anode; (iii) destabilization of the Ni–YSZ/YSZ interface due to materials transport toward LSCF anode. This post-test analysis is in accordance with Schefold's impedance diagram analysis mentioned above [112].

4.3. Stack

The use of EIS to analyze stack cells is quite limited. As a matter of fact, very few works can be found in the literature [115–119]. Nevertheless, some studies are worth mentioning.

In the first study considered here, Ebbesen et al. focused on both electrolysis of H₂O and co-electrolysis of H₂O and CO₂ [117]. The LSM–YSZ/YSZ/Ni–YSZ cell was tested for up to about 1200 h with different current densities applied (from -0.20 A cm^{-2} to -0.75 A cm^{-2}). Gas was supplied as received for H₂O electrolysis while it was cleaned for co-electrolysis of H₂O and CO₂. In the case of H₂O electrolysis, an increase in R_s with time was observed, surely due to degradation of contacting between the cells and the interconnect plates. An R_p increase was observed as well, meaning degradation of electrochemical processes. Hence, analysis of the impedance data, using the ADIS method in this study, allowed noticing that degradation was characterized by a relaxation frequency around 100–300 Hz, as observed before for a similar cell but in a single cell configuration [47,99–101]. Hence, since gases were supplied as received, it is once again concluded that degradation was at least partly caused by blockage of the active TPBs because of gas impurities. In the case of co-electrolysis, no R_p

Table 3

Main experimental conditions and cell degradation obtained during operation for the papers discussed in Section 4.

Ref.	Cell configuration	O ₂ Electrode	Electrolyte	H ₂ electrode	Active area (cm ²)	Temperature (°C)	Frequency range Amplitude signal Fitting with EEC	Parameters studied using EIS	Electrolysis test time	Current density applied for degradation test (A cm ⁻²)	Cell degradation (%/1000 h or mV/1000 h)
[88]	Symmetrical	LSM	YSZ (support)	LSM	0.8	840	200 kHz–0.1 Hz 10 mV No	Time	100 h	—	—
[89]	Symmetrical	LSM	YSZ (support)	LSM	0.5	800	100 kHz–0.1 Hz — Yes	Time	48 h	−0.5	—
[92]	Symmetrical	LSM–YSZ	YSZ (support)	LSM–YSZ	0.5	650, 700, 750 and 800	100 kHz–0.1 Hz 10 mV Yes	Time Temperature	100 h	−0.5	—
[96]	Symmetrical	LSM–GDC	YSZ (support)	LSM–GDC	0.5	650, 700, 750 and 800	100 kHz–0.1 Hz 10 mV Yes	Time Temperature Pd loading	100 h	−0.2	—
[99]	Single	LSM–YSZ	YSZ	Ni–YSZ (support)	16	750, 850 and 950	82 kHz–0.82 Hz 12 mV No	Time	up to 766 h	−0.25 and −0.5	—
[100]	Single	LSM–YSZ	YSZ	Ni–YSZ (support)	16	850 and 950	82 kHz–0.82 Hz 12 mV No	Time	up to 1600 h	0, −0.5 and −1	—
[101]	Single	LSM–YSZ	YSZ	Ni–YSZ (support)	16	850 and 950	82 kHz–0.82 Hz 12 mV Yes	Time	up to 1510 h	−0.5	—
[47]	Single	LSM–YSZ	YSZ	Ni–YSZ (support)	16	850	82 kHz–0.82 Hz — No	Time H ₂ O electrode gas composition	up to 1340 h	−0.25 and −0.5	—
[104]	Single	LSM–YSZ	YSZ	Ni–YSZ (support)	—	750, 800 and 850	82 kHz–0.82 Hz 60 mA No	Time H ₂ O electrode gas composition Temperature	up to 382 h	−0.25, −0.5 and −1	—
[105]	Single	LSM–YSZ	YSZ	Ni–YSZ (support)	—	850	82 kHz–0.82 Hz — Yes	Time	up to 900 h	−1, −1.5 and −2	—
[106]	Single	LSM–YSZ	YSZ	Ni–YSZ (support)	16	800 and 850	82 kHz–0.82 Hz — No	Time	up to 932 h	−1 and −1.5	—
[111]	Single	LSM	YSZ	Ni–YSZ (support)	45	Between 800 and 900	20 kHz–0.01 Hz 40 mA cm ⁻² RMS No	Time H ₂ O electrode gas composition	up to about 1000 h	−1 and −1.5	From 2%/1000 h (0.3 A cm ⁻² applied) to 16%/1000 h (0.5 A cm ⁻² applied)
[112,114]	Single	LSCF	YSZ	Ni–YSZ (support)	45	About 780	20 kHz–0.1 Hz 20–40 mA cm ⁻² RMS No	Time	9000 h	−1	3.8%/1000 h
[117]	6-cell stack and 10-cell stack	LSM–YSZ	YSZ	Ni–YSZ (support)	92.16	800, 850 and 900	50 kHz–0.2 Hz — No	Time	up to 1500 h	−0.2, −0.25, −0.5 and −0.75	From 9 mV/1000 h to 240 mV/1000 h
[118]	5-cell stack	LSM–YSZ	YSZ	Ni–YSZ (support)	100	About 800	— — No	Time	2651 h	−0.4, −0.6 and −0.8	About 3%/1000 h for the inner cells
[119]	5-cell stack	LSM–YSZ	YSZ (support)	Ni–CGO	100	820	10 kHz–0.1 Hz ~30 mV No	Time	4055 h	−0.4	5.6%/1000 h (average)
[120]	Microtubular	LSM–YSZ	YSZ	Ni–YSZ (support)	—	750, 820, 895 and 950	10 kHz–0.1 Hz 100 mV Yes	H ₂ O electrode gas composition	—	From −2.5 to 0.5	—

(continued on next page)

Table 3 (continued)

Ref.	Cell configuration	O ₂ Electrode	Electrolyte	H ₂ electrode	Active area (cm ²)	Temperature (°C)	Frequency range	Amplitude signal fitting with EEC	Parameters studied using EIS	Electrolysis test time	Current density applied for degradation test (A cm ⁻²)	Cell degradation (%/1000 h or mV/1000 h)
[121]	Single	LSM–YSZ	YSZ	Ni–YSZ (support)	45	Between 800 and 900	10 kHz–0.01 Hz 10–30 mA cm ⁻² RMS	Yes	Time H ₂ O electrode gas composition	About 1000 h	-0.34 and -0.5	—
[123]	Single	LSCF–GDC	YSZ	Ni–YSZ (support)	45	About 700	100 kHz–0.1 Hz	—	Current density applied Time	600 h	-0.444 (steady state cond.) 0, -0.022 and -0.444 (transient cond.)	—
[124]	Single	LSM	YSZ	Ni–YSZ (support)	45	800 and 900	30 kHz–0.1 Hz 1–2 A RMS	no	H ₂ O electrode gas composition	160 h	-0.5	—
[127]	Button	LSM	YSZ	Ni–YSZ (support)	—	800	1 MHz–0.1 Hz 10 μA RMS	Yes	Current density applied Temperature	—	—	—
[128]	Single	LSCF	YSZ	Ni–YSZ (support)	3.14	650, 700 and 800	10 kHz–0.01 Hz 30 mA	Yes	H ₂ O electrode gas composition	—	—	—
									Current density applied temperature	—	—	—
									H ₂ O electrode gas flow rate	—	—	—
									P _{O₂} at the O ₂ electrode	—	—	—

increase was observed, which means no electrode processes degradation, confirming once again that cleaning the inlet gases allows avoiding at least partly degradation of the cells [47], even in a stack configuration. In the second study, Brisse et al. tested a 5-cell stack with cells similar to what used in the work reported above [99] for more than 2600 h [118]. Even if impedance spectroscopy measurements included only the first 700 h, two interesting information were obtained. First, a shift of the HF part of the impedance diagram (f_{HF} around 100 Hz) typically associated to interfacial charge transfer [50,120–122,124,128] was observed. Indeed, as for Hauch et al. [99], increase followed by decrease in R_{HF} was observed with time, assimilated to passivation and activation of the stack, respectively. Second, reduction of a leaking at the H₂O supply tubing within this time period led to the decrease in the LF part of the impedance diagram (f_{LF} around 3 Hz) attributed to gas diffusion at the H₂ electrode. However, it would have been even more interesting to acquire impedance measurements concerning the additional period of test. In the third study, Schefold et al. considered a 5-cell stack composed by a commercial LSCF/YSZ/Ni–CGO cell [119]. The stack was tested for 4055 h, applying -0.4 A cm^{-2} . In this case, only an increase in R_s was observed with time. Since no electrolyte degradation was observed in the post-test analysis, it surely means that degradation of the contact at the cell interconnects occurred during the test. Moreover, impedance data analysis revealed no change in the two phenomena suggested by the authors, interfacial charge transfer and gas diffusion.

4.4. Original papers on SOEC degradation study by EIS

The following part mentions studies that address SOEC degradation in an unusual way, either the configuration of the system, the physical degradation process studied or the adopted analysis approach.

In the first study, Laguna-Bercero et al. considered the degradation of a Ni–YSZ/YSZ/LSM–YSZ cell in a microtubular configuration at high current densities (up to -2.5 A cm^{-2}) and for different water vapor partial pressures (P_{H_2O}) [120]. A quite surprising observation was made from impedance diagrams measured at OCV with different P_{H_2O} : indeed, changing P_{H_2O} led to an increase in R_s . Since R_s is independent of P_{H_2O} , this increase is a consequence of YSZ degradation most probably due to the operation under high current densities. Furthermore, the use of an EEC allowed separating R_p into two terms R_{HF} and R_{LF} . R_{HF} which remained almost constant with P_{H_2O} variation, was related to electrode reactions [77,104,124,128] whereas R_{LF} , which decreased with P_{H_2O} increase, was assigned to gas diffusion [77,104,124,128]. Additional evidence of YSZ degradation was observed from impedance diagrams recorded at OCV before and after a test operated under extreme conditions ($T = 895^\circ\text{C}$ and -1.75 A cm^{-2} applied). Indeed, only 10 min of test led to an irreversible degradation of YSZ electrolyte characterized by a 63% increase in R_s while R_p remained almost unchanged. Post-test analysis of the cell using SEM and EDS showed other evidences of YSZ degradation such as presence of voids and cracks at the grain boundaries of the YSZ electrolyte close to LSM–YSZ electrode.

In the second study, Schefold et al. investigated the electronic conduction of YSZ electrolyte considering a LSM–YSZ/YSZ/Ni–YSZ cell [121]. Identification of YSZ electronic conduction was allowed by comparison of the impedance diagrams measured with and without H₂O supply. When H₂O was supplied to the cell (50% in this study), two contributions could be observed: a HF contribution with a relaxation frequency at 1 kHz associated to charge transfer at both electrode/electrolyte interfaces [46,50,122,124,128], and a LF contribution with a peak at 2 Hz related here to H₂O conversion

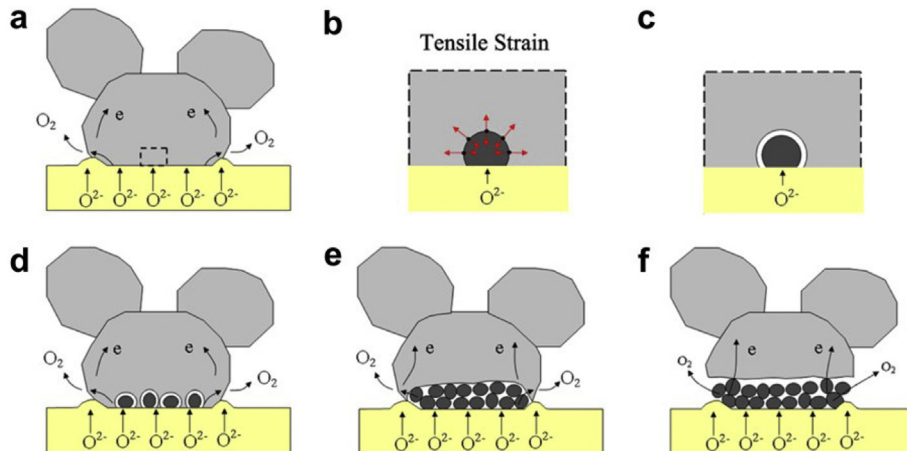


Fig. 7. Schematic illustrations of the microstructural change of the LSM oxygen electrode/YSZ electrolyte interface under SOEC operation conditions: (a) oxygen migration from YSZ electrolyte to LSM grain bulk at the interface, (b) local tensile strains within LSM particles due to the shrinkage of LSM lattice, (c) local tensile strains induced microcrack formation, (d) formation of individual nanoparticles, (e) propagation and continuous nanoparticles formation and LSM grain is bonded to YSZ electrolyte through bridges along edge of the convex contact ring, and (f) formation of complete nanoparticle layers and delamination of the LSM oxygen electrode under high internal oxygen partial pressure at the interface. According to Ref. [89]. Elsevier permission.

[50,86] whereas this contribution is usually attributed to gas diffusion at the H₂ electrode [104,124,128]. Hence, when no H₂O was supplied, a shift of the LF contribution from 2 Hz to up to 30 Hz was noticed, depending on the current density applied. Besides, in such condition, increasing the current density led to a decrease in the impedance diagram at all frequencies, meaning a decrease in the resistance to electronic conduction of the YSZ electrolyte.

In the last study discussed in this part, Petipas et al. tested a commercial LSCF–GDC/YSZ/Ni–YSZ cell for 600 h [123]. The singularity of this study is that electric transient operations are included in the test, which is of particular interest for the possible coupling of SOECs with intermittent sources of energy such as solar cells and wind turbines. Transient tests consisted in 1800 square waves applied over 140 cumulated hours, with an applied current of −1 A and −20 A as well as 0 A and −20 A. In this case, as shown Fig. 12, R_p was separated into three contributions: R_{HF} with a relaxation frequency $f_{HF} = 3.5$ kHz, R_{MF} with $f_{MF} = 70$ Hz and R_{LF} with $f_{LF} = 2$ Hz. Moreover, as shown in Fig. 12, evolution of the cell behavior with time (500 h) by EIS led here to the following

observations: cell degradation occurred with time, mainly characterized by an increase in both R_s and R_{MF} which could not be clearly ascribed to a phenomenon. In the meantime, R_{LF} associated to gas diffusion at the Ni–YSZ electrode was found to remain almost unchanged. Even if R_{HF} showed almost no variation globally, important value changes could be noticed with time (more particularly between $t = 300$ h and $t = 400$ h), which makes difficult to conclude for this contribution usually associated to interfacial charge transfer [50,104,120,124,128]. Hence, further investigations are needed to have a better understanding on transient conditions of operation on the SOE cell behavior. Nevertheless, this very interesting work showed that SOECs can be operated under on–off conditions without important degradation, making possible its coupling with intermittent energy sources.

5. Systematic EIS analysis of SOEC

It is quite surprising to notice that not many studies have been reported so far in literature on the systematic EIS analysis of SOE single cell with the variation of experimental parameters such as current density, temperature, P_{H_2O}/P_{H_2} ratio or gas flow rate. The following papers discussed below are, with the ones already discussed earlier [47,92,96,111], the only studies found in the literature

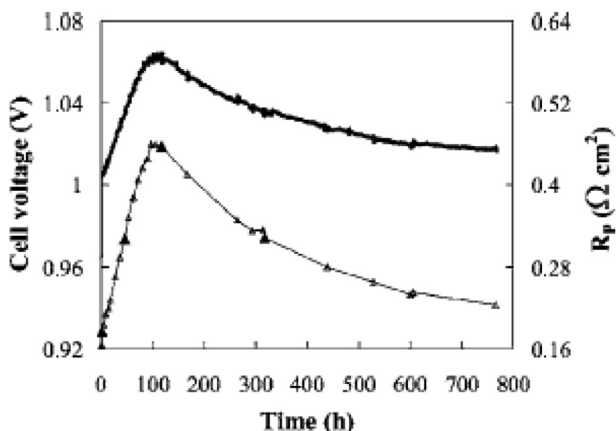


Fig. 8. Ni–YSZ/YSZ/LSM–YSZ cell voltage and polarization resistance R_p (Δ) as a function of time. Experimental conditions were constant at -0.25 A cm^{-2} , 850°C , $P_{H_2O}/P_{H_2} = 7$ at the H₂ electrode and oxygen was passed over the O₂ electrode. Closed symbols for R_p correspond to the impedance spectra shown in Fig. 9. According to Ref. [99]. Elsevier permission.

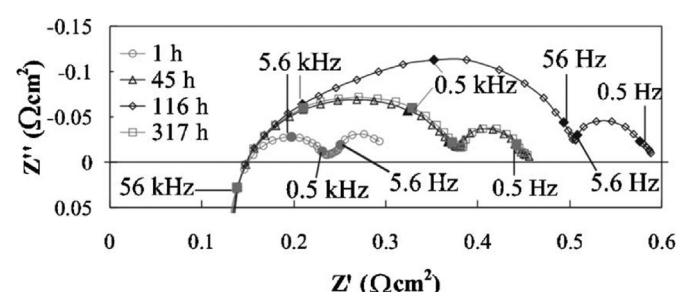


Fig. 9. Impedance spectra recorded after 1, 45, 116 (max R_p), and 317 h of electrolysis for the Ni–YSZ/YSZ/LSM–YSZ cell at constant conditions (850°C , -0.25 A cm^{-2} , $P_{H_2O}/P_{H_2} = 7$, under O₂). The spectrum recorded after 45 h of electrolysis was during passivation of the cell while the spectrum recorded after 317 h of electrolysis was during the subsequent activation of the cell that happened over time at the same constant electrolysis conditions as during the initial passivation. According to Ref. [99]. Elsevier permission.

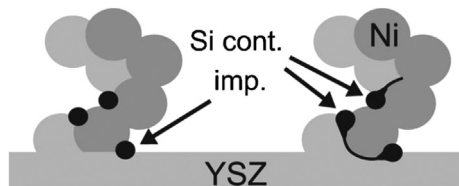


Fig. 10. Schematic presentation of Si-containing impurities segregating to the H_2O electrode/electrolyte interface during electrolysis as observed by SEM. The impurities tend to block the 3 PB, or also segregate to the 2 PB between the Ni and the YSZ. According to Ref. [100]. Elsevier permission.

so far with such an approach. In the first paper, Brisse et al. studied the influence of current density, P_{H_2O}/P_{H_2} and temperature on cell behavior [124]. They considered a commercial LSM/YSZ/Ni–YSZ cell. In this case, three contributions could be distinguished as part of R_p : R_{HF} between 10,000 and 100 Hz, R_{MF} between 100 and 10 Hz, and R_{LF} between 10 and 1 Hz. Besides, a decrease in all three contributions with increasing temperature was observed, meaning that there are thermally activated. Moreover, impedance measurements for different current densities applied and different P_{H_2O}/P_{H_2} ratios allowed identifying two contributions: R_{HF} , which increases with increasing current densities applied, was related to charge transfer at the electrode/electrolyte interface [47,50,104,120,128] while R_{LF} was associated to gas diffusion at the H_2 electrode since it decreases with increasing P_{H_2O}/P_{H_2} ratio [77,104,120,128]. In the second paper, Graves et al. examined the change in temperature and gas composition on a LSM–YSZ/YSZ/Ni–YSZ cell used for co-electrolysis of H_2O and CO_2 [104]. In this case, impedance data analysis with the DRT approach led to the determination of five summit frequencies. Hence, based on the model developed by Barfod et al. [102,125], five rate limiting processes could be identified (from higher to lower frequencies): a first LSM–YSZ electrode process independent of any gas changes, a Ni–YSZ electrode process, a second LSM–YSZ electrode process, and two low frequency processes mainly at the Ni–YSZ side of the cell independent of temperature and ascribed to gas conversion and gas diffusion [107,108,126]. In the same paper, a study on cell degradation was also done, as previously discussed (see Section 4.2).

It is also interesting to mention the work realized by Laguna-Bercero et al. who studied the electrolyte degradation including

by means of the influence of P_{H_2O}/P_{H_2} ratio in a tubular cell configuration [84], or Schefold et al. who focused on the possible electronic conduction of YSZ electrolyte, considering especially the influence of current density applied [121]. These studies were discussed in more details before (see Section 4.4).

The next paper reports a recent work published by Shin et al. on a LSM/YSZ/Ni–YSZ cell [127]. This work is very interesting through several points. Firstly, the inductive loop usually observed on impedance diagrams and attributed to wiring artifacts was modeled here by an inductance–resistance parallel circuit, with the resistance proportional to the inductance. Secondly, study of the cell with the change in the current density applied and P_{H_2O}/P_{H_2} ratio, coupled to the use of an equivalent circuit including ideal Gerischer element, allowed the deconvolution of three main contributions to polarization losses: a charge transfer impedance of Ni–YSZ electrode, a “kinetics co-limited by surface diffusion and desorption” impedance of LSM electrode, and a gas diffusion impedance of Ni–YSZ electrode. Increase in both Ni–YSZ impedances and decrease in LSM impedance were observed with increasing current densities applied. Moreover, the LSM contribution was further investigated using a finite-length Gerischer element composed by three independent parameters including the adsorption capacitance C_p , which allowed a better understanding on the influence of current density and P_{H_2O}/P_{H_2} on the surface diffusivity D , the ad/desorption coefficient k and the utilization length l_δ , all related to the LSM electrode. Hence, it was found that (i) decrease in the LSM contribution, represented as $(C_p(kD)^{1/2})^{-1}$, can be ascribed to the increase in C_p , D and k ; (ii) for lower ratio $P_{H_2O}/P_{H_2} = 3$, the decrease in the LSM contribution is mainly due to the increase in both D and C_p ; (iii) for higher ratio $P_{H_2O}/P_{H_2} = 5$, the decrease is mainly associated to the increase in C_p . Last interesting point, estimation of $D = 2 \times 10^{-4} \text{ cm}^2 \text{ s}^{-1}$, $k = 10^3 \text{ s}^{-1}$ and $l_\delta = 5 \mu\text{m}$ was deduced from the finite-length Gerischer model, representing the effective values of the LSM–YSZ functional layer with a thickness of about 10 μm .

In the last paper of this part, the SOE cell is studied considering an important number of parameters. Indeed, in this study by Néchache et al., EIS and chronopotentiometry were combined in order to characterize the electrochemical performance and behavior of a commercial LSCF/YSZ/Ni–YSZ cell through the analysis of current density, temperature, P_{H_2O}/P_{H_2} ratio, H_2O electrode gas flow rate and P_{O_2} at the O_2 electrode [128]. Hence, analysis of these experimental parameters coupled with the use of EEC allowed the deconvolution of the measured impedance diagrams into three or four arcs, each of them characterized by specific capacitance and relaxation frequency. Thus, each arc could be ascribed to a phenomenon directly related to the electrochemical reactions or cell degradation. In this case, in accordance with literature [50,111,120–122,124], impedance diagram analyses conducted to the following identification: (i) the HF arc, mainly influenced by temperature and current density, and characterized by $\{C_{HF} = 1 \text{ mF cm}^{-2}, f_{HF} = 100 \text{ Hz}\}$ was related to charge transfer at the electrode/electrolyte interface; (ii) the LF arc, mainly influenced by current density, P_{H_2O}/P_{H_2} ratio and H_2 electrode gas flow rate, and characterized by $\{C_{LF} = 10 \text{ F cm}^{-2}, f_{LF} = 0.1 \text{ Hz}\}$ was attributed to gas diffusion at the H_2 electrode. Furthermore, the MF part of the impedance diagram was constituted by one or two arcs, depending on the experimental conditions of the cell. The corresponding capacitance and relaxation frequency orders of magnitude were $\{C_{MF} = 0.1 \text{ F cm}^{-2}, f_{MF} = 1 \text{ Hz}\}$ when one arc was considered and $\{C_{MF1} = 0.1 \text{ F cm}^{-2}, f_{MF1} = 10 \text{ Hz}; C_{MF2} = 0.5 \text{ F cm}^{-2}, f_{MF2} = 1 \text{ Hz}\}$ when two arcs were considered. According to the fact that this MF part was varying with current density, P_{H_2O}/P_{H_2} ratio and H_2 electrode gas flow rate, and based on the literature, these values could be ascribed to gas diffusion at the O_2 electrode [109] and/or to O_2^{2-}

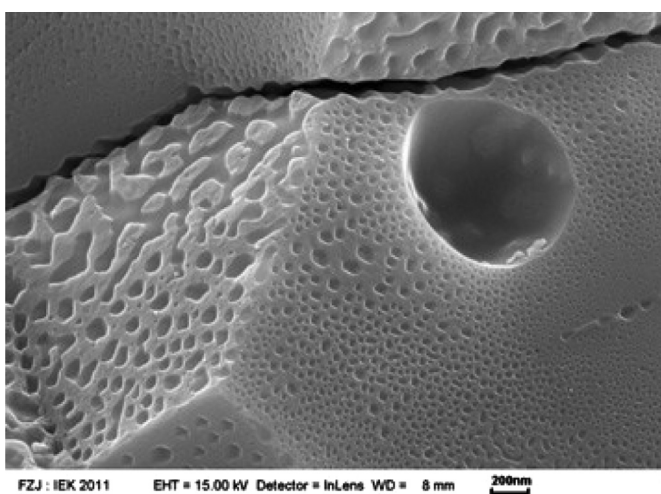


Fig. 11. SEM image of fracture surfaces and pores formation at the YSZ electrolyte grain as a consequence of the degradation test on the Ni–YSZ/YSZ/LSCF cell for 9000 h at about 780 °C and -1 A cm^{-2} . According to Ref. [114]. Elsevier permission.

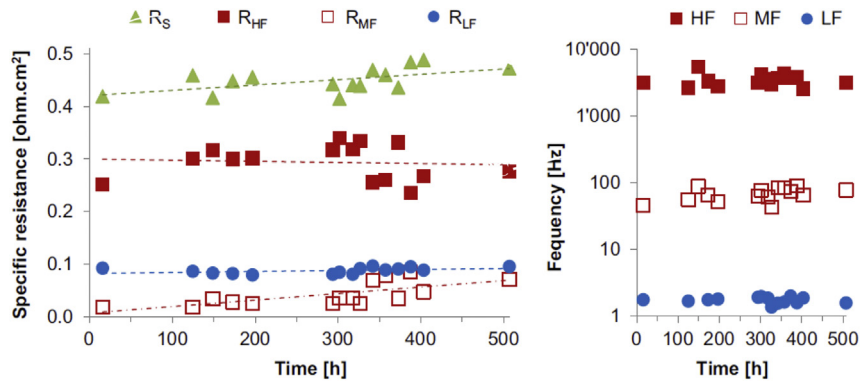


Fig. 12. Evolution of the area specific resistances of the modeled equivalent circuits (left) and their corresponding relaxation frequencies (right) during testing of the Ni–YSZ/YSZ/GDC–LSCF cell at about 700 °C. According to Ref. [123]. Elsevier permission.

ion transport through the O₂ electrode [109] and/or gas conversion at the H₂ electrode [99,101,105,107]. Thus, further studies are required to clearly ascribe the MF part of the impedance diagram to one or several of the mentioned phenomena. Moreover, even if some of the phenomena were not fully identified, it is very interesting to deduce from Fig. 13a and b that the phenomena influencing the studied cell were characterized by capacitances and relaxation frequencies with different orders of magnitude, meaning that applying this approach clearly allowed distinguishing the main phenomena governing the SOEC, at short term in this case. Hence, this work constitutes a first and important step for the systematic *in-situ* diagnosis by EIS of SOEC reaction mechanisms and degradation.

6. Conclusive remarks

This review has evidenced how EIS can be used as a diagnosis tool of SOEC performance and degradation. Indeed, this review has firstly shown the ability of EIS to characterize SOEC electrodes' performance and mechanisms. Furthermore, it has been established that the use of this *in-situ* fundamental tool during SOEC testing additionally to post-test characterization methods allows going further into the understanding of the processes explaining SOEC degradation for symmetrical, single and stack cell configurations, for both short- and long-term studies. However, a thorough understanding of SOEC functioning and degradation processes is still needed to reach commercially viable performances for both short- and long-term potential applications. Therefore, as shown in this review through a few examples, a possible answer to this requirement might be the deeper development of a systematic EIS analysis of SOEC with the variation of experimental parameters such as temperature, current density or gas composition. Nevertheless, the studies discussed in this review show that this approach has to be improved in several ways. To begin with, as explained earlier, combination of DRT or ADIS with EEC is strongly recommended. This has almost not been done so far. Besides, the characteristic values obtained from impedance diagrams fitting by EEC should be more often mentioned in the papers and further discussed, for instance, by establishing correlations between this characteristic values and the identified electrochemical processes or by discussing how they answer to the variation of a parameter. In addition, reliability of impedance data interpretation can be questionable when associations of characteristic values to electrochemical processes are only based on results obtained in a SOFC configuration, which is close in some ways to a SOEC configuration but still different, including in terms of reaction mechanisms. Thus,

once improved and generalized, extension of this approach to different kind of cells (composition, microstructure, dimension, etc...) can thus lead to the set-up of a strong database for the identification of the main phenomena explaining SOEC functioning and degradation.

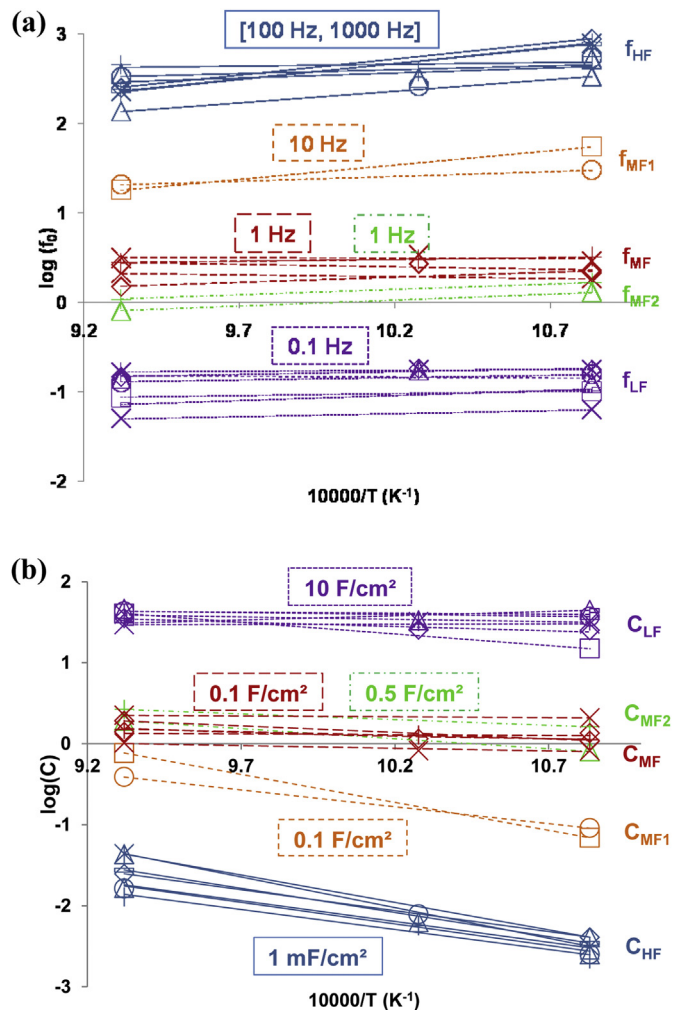


Fig. 13. Arrhenius plots showing relaxation frequency (a) and capacitance (b) orders of magnitude obtained through this study. Measurements were performed on the Ni–YSZ/YSZ/LSCF cell for $P_{\text{H}_2\text{O}}/P_{\text{H}_2} = 9$ (H₂O electrode), air (O₂ electrode), H₂O electrode gas flow rate $\times 1^*$. $^* = 2.26$ NL/h. According to Ref. [128].

Acknowledgments

This work is supported by the French Research National Agency (ANR) through *Hydrogène et piles à combustible* program (project FIDELHYO n°ANR-09-HPAC-005).

References

- [1] X.M.A. Laguna-Bercero, J. Power Sourc. 203 (2012) 4–16.
- [2] National Academy of Sciences, National Research Council, The Hydrogen Economy: Opportunities, Costs, Barriers, and R&D Needs, National Academy of Sciences, National Research Council, February 2004.
- [3] M.N. Manage, D. Hodgson, N. Milligan, S.J.R. Simons, D.J.L. Brett, Int. J. Hydrogen Energy 36 (2011) 5782–5796.
- [4] W. Döñitz, R. Schmidberger, E. Steinheil, Int. J. Hydrogen Energy 5 (1980) 55–63.
- [5] G.W. Fischer, H.B. Gels, F. Gross, K. Liemert, F.J. Rohr, J. Power Sourc. 3 (1978) 331–345.
- [6] Elektrochemische Prozesse, DECHEMA-Studie, 1975.
- [7] A.O. Isenberg, L.E. Brecher, Water vapor electrolysis at high temperatures, Westinghouse Electric Corp., Final Report, Project Fuel Cell, Rep. No. 57 (1970), in: Proc. First Int. Energy Agency Water Electrolysis Workshop, Brookhaven National Laboratory, Sept. 1975.
- [8] F.J. Rohr, High temperature solid oxide fuel cells, in: Proc. Int. Energy Agency Workshop on Solid Electrolyte Fuel Cells, Brookhaven National Laboratory, May 1977.
- [9] S.P.S. Badwal, Solid State Ionics 52 (1992) 23–32.
- [10] A.O. Isenberg, Solid State Ionics 3/4 (1981) 431–437.
- [11] N.J. Maskalick, Int. J. Hydrogen Energy 11 (1986) 563–570.
- [12] G. Imarisio, Int. J. Hydrogen Energy 6 (1986) 153–158.
- [13] G.B. Barbi, C.M. Mari, Mater. Chem. 6 (1981) 35–54.
- [14] G.B. Barbi, C.M. Mari, Solid State Ionics 6 (1982) 341–351.
- [15] G.B. Barbi, C.M. Mari, in: Paper Presented at the 4th Int. Conf. on Solid State Ionics, Grenoble, 4–8 July 1983.
- [16] G.B. Barbi, C.M. Mari, Solid State Ionics 26 (1988) 243–250.
- [17] G.B. Barbi, C.M. Mari, Int. J. Hydrogen Energy 9 (1984) 895–899.
- [18] E.J.L. Schouler, Solid State Ionics 9–10 (1983) 945–952.
- [19] F.J. Salzano, G. Skaperdas, A. Mezzina, Int. J. Hydrogen Energy 10 (1985) 801–809.
- [20] W. Döñitz, R. Schmidberger, Int. J. Hydrogen Energy 7 (1982) 321–330.
- [21] W. Döñitz, E. Erdle, Int. J. Hydrogen Energy 10 (1985) 291–295.
- [22] W. Döñitz, G. Dietrich, E. Erdle, R. Streicher, Int. J. Hydrogen Energy 13 (1988) 282–287.
- [23] K.H. Quandt, R. Streicher, Int. J. Hydrogen Energy 11 (1986) 309–315.
- [24] H. Arashi, H. Naito, H. Miura, Int. J. Hydrogen Energy 16 (1991) 603–608.
- [25] K. Eguchi, T. Hatagishi, H. Arai, Solid State Ionics 86–88 (1996) 1245–1249.
- [26] A. Momma, T. Kato, Y. Kaga, S. Nagata, J. Ceram. Soc. Jpn. 105 (1997) 369–373.
- [27] K.V. Jensen, R. Wallenberg, I. Chorkendorff, M. Mogensen, Solid State Ionics 160 (2003) 27–37.
- [28] R. Hino, K. Haga, H. Aita, K. Sekita, Nucl. Eng. Des. 233 (2004) 363–375.
- [29] N. Osada, H. Uchida, M. Watanabe, J. Electrochem. Soc. 153 (2006) A816–A820.
- [30] M.S. Sohal, J.E. O'Brien, C.M. Stoots, V.I. Sharma, B. Yildiz, A. Virkar, in: Proceedings of the ASME Fuel Cell, 2010, pp. 1–11.
- [31] C. Stoots, R. O'Brien, T. Cable, J. O'Brien, in: Proceedings of the 9th European SOFC Forum, 2010 (Chapter 14), pp. 14–21.
- [32] J.E. O'Brien, C.M. Stoots, in: Proceedings of the 9th European SOFC Forum, 2010 (Chapter 14), pp. 14–27.
- [33] V.I. Sharma, B. Yildiz, J. Electrochem. Soc. 157 (2010) B441–B448.
- [34] R. Knibbe, S.D. Ebbesen, M. Mogensen, ECS Trans. 28 (2010) 77–87.
- [35] Y. Zhang, K. Chen, C. Xia, S.P. Jiang, M. Ni, Int. J. Hydrogen Energy 37 (2012) 13914–13920.
- [36] M.E. Orazem, B. Tribollet, *Electrochemical Impedance Spectroscopy*, J. Wiley & Sons, Hoboken, New Jersey, 2008.
- [37] V.F. Lvovich, *Impedance Spectroscopy*, J. Wiley & Sons, Hoboken, New Jersey, 2008.
- [38] E. Barsoukov, J.R. MacDonald, *Impedance Spectroscopy*, J. Wiley & Sons, Hoboken, New Jersey, 2005.
- [39] C.W. Carter, Bell Syst. Tech. J. 4 (1925) 387–401.
- [40] K.S. Cole, R.H. Cole, J. Chem. Phys. 9 (1941) 341–351.
- [41] J.E.B. Randles, Discuss. Faraday Soc. 1 (1947) 11–19.
- [42] G. Jaffé, Phys. Rev. 85 (1952) 354–363.
- [43] H. Chang, G. Jaffé, J. Chem. Phys. 20 (1952) 1071–1077.
- [44] J.R. Macdonald, Phys. Rev. 92 (1953) 4–17.
- [45] R.J. Friauf, J. Chem. Phys. 22 (1954) 1329–1338.
- [46] S.H. Jensen, A. Hauch, P.V. Hendriksen, M. Mogensen, N. Bonanos, T. Jacobsen, J. Electrochem. Soc. 154 (2007) B1325–B1330.
- [47] S.D. Ebbesen, C. Graves, A. Hauch, S.H. Jensen, M. Mogensen, J. Electrochem. Soc. 157 (2010) B1419–B1429.
- [48] H. Schichlein, A.C. Müller, M. Voigts, A. Krügel, E. Ivers-Tiffée, J. Appl. Electrochem. 32 (2002) 875–882.
- [49] J.E. Bauerle, J. Phys. Chem. Solids 30 (1969) 2657–2670.
- [50] A. Leonide, V. Sonn, A. Weber, E. Ivers-Tiffée, J. Electrochem. Soc. 155 (2008) B36–B41.
- [51] Q. Liu, C. Yang, X. Dong, F. Chen, Int. J. Hydrogen Energy 35 (2010) 10039–10044.
- [52] Z. Yang, C. Jin, C. Yang, M. Han, F. Chen, Int. J. Hydrogen Energy 36 (2011) 11572–11577.
- [53] W. Zhu, D. Ding, C.R. Xia, Electrochem. Solid State Lett. 11 (2008) B83–B86.
- [54] E.P. Murray, T. Tsai, S.A. Barnett, Nature 40 (1999) 649–651.
- [55] J.H. Piao, K.N. Sun, N.Q. Zhang, S. Xu, J. Power Sourc. 175 (2008) 288–295.
- [56] S.P. Simmer, J.R. Bonnett, N.L. Canfield, K.D. Meinhardt, J.P. Shelton, V.L. Sprenkle, J.W. Stevenson, J. Power Sourc. 113 (2003) 1–10.
- [57] R. Chiba, F. Yoshimura, Y. Sakurai, Solid State Ionics 152–153 (2002) 575–582.
- [58] S.P. Simmer, J.R. Bonnett, N.L. Canfield, K.D. Meinhardt, V.L. Sprenkle, J.W. Stevenson, Electrochem. Solid State Lett. 5 (2002) A173–A175.
- [59] Y. Teraoka, H.M. Zhang, K. Okamoto, N. Yamazoe, Mater. Res. Bull. 23 (1988) 51–58.
- [60] J.W. Stevenson, T.R. Armstrong, R.D. Carneim, L.R. Pederson, W.J. Weber, J. Electrochem. Soc. 143 (1996) 2722–2729.
- [61] J. Fleig, J. Power Sourc. 105 (2002) 228–238.
- [62] S.B. Adler, J.A. Lane, B.C.H. Steele, J. Electrochem. Soc. 143 (1996) 3554–3564.
- [63] J.A. Kilner, R.A. De Souza, I.C. Fullarton, Solid State Ionics 86–88 (1996) 703–709.
- [64] P. Stevens, C. Lalanne, J.M. Bassat, F. Mauvy, J.C. Grenier, France Brevet, 2004, FR 2872174.
- [65] E. Boehm, J.M. Bassat, P. Dordor, F. Mauvy, J.C. Grenier, P. Stevens, Solid State Ionics 176 (2005) 2717–2725.
- [66] F. Chauveau, J. Mougin, J.M. Bassat, F. Mauvy, J.C. Grenier, J. Power Sourc. 195 (2010) 744–749.
- [67] T. Ogier, F. Chauveau, J.M. Bassat, F. Mauvy, J. Mougin, J.C. Grenier, in: Fundamentals and Developments of Fuel Cells Conference, Grenoble, 2011.
- [68] M. Mori, T. Yamamoto, H. Itoh, H. Inaba, H. Tagawa, J. Electrochem. Soc. 145 (1998) 1374–1381.
- [69] P.K. Patro, T. Delahaye, E. Bouyer, P.K. Sinha, Int. J. Hydrogen Energy 37 (2012) 3865–3873.
- [70] S.P.S. Badwal, F.T. Ciacchi, D. Milosevic, Solid State Ionics 136 (2000) 91–99.
- [71] T.I. Politova, J.T.S. Irvine, Solid State Ionics 168 (2004) 153–165.
- [72] S.W. Tao, J.T.S. Irvine, J. Electrochem. Soc. 151 (2004) A252–A259.
- [73] S.W. Tao, J.T.S. Irvine, Nat. Mater. 2 (2003) 320–323.
- [74] W. Wang, L. Zhang, S.P. Jiang, J. Power Sourc. 178 (2008) 92–96.
- [75] X.D. Yang, J.T.S. Irvine, J. Mater. Chem. 18 (2008) 2349–2354.
- [76] F. Bidrawn, G. Kim, G. Corre, J.T.S. Irvine, J.M. Vohs, R.J. Gorte, Electrochem. Solid State Lett. 11 (2008) B167–B170.
- [77] C. Jin, C. Yang, F. Zhao, D. Cui, F. Chen, Int. J. Hydrogen Energy 36 (2011) 3340–3346.
- [78] A. Ringuedé, S. Awamat, M. Cassir, L. Dessemont, S. Tadokoro, E. Lay, C. Steil, R. Laucourtin, K. Couturier, in: Fundamentals and Developments of Fuel Cells Conference, Grenoble, 2011.
- [79] C. Bernuy-Lopez, R. Knibbe, Z. He, X. Mao, A. Hauch, K.A. Nielsen, J. Power Sourc. 196 (2011) 4396–4403.
- [80] C. Yang, A. Coffin, F. Chen, Int. J. Hydrogen Energy 35 (2010) 3221–3226.
- [81] B. Yu, W. Zhang, J. Xu, J. Chen, Int. J. Hydrogen Energy 33 (2008) 6873–6877.
- [82] M. Liang, B. Yu, M. Wen, J. Chen, J. Xu, Y. Zhai, J. Power Sourc. 190 (2009) 341–345.
- [83] M.A. Laguna-Bercero, J.A. Kilner, S.J. Skinner, Chem. Mater. 22 (2010) 1134–1141.
- [84] M.A. Laguna-Bercero, J.A. Kilner, S.J. Skinner, Solid State Ionics 192 (2011) 501–504.
- [85] P. Kim-Lohsoontorn, D.J.L. Brett, N. Laosiripojana, Y.-M. Kim, J.-M. Bae, Int. J. Hydrogen Energy 35 (2010) 3958–3966.
- [86] W. Wang, Y. Huang, S. Jung, J.M. Vohs, R.J. Gorte, J. Electrochem. Soc. 153 (2006) A2066–A2070.
- [87] M. Liang, B. Yu, M. Wen, J. Chen, J. Xu, Y. Zhai, Int. J. Hydrogen Energy 35 (2010) 2852–2857.
- [88] M. Keane, M.K. Mahapatra, A. Verma, P. Singh, Int. J. Hydrogen Energy 37 (2012) 16776–16785.
- [89] K. Chen, S.P. Jiang, Int. J. Hydrogen Energy 36 (2011) 10541–10549.
- [90] S.P. Jiang, J.P. Zhang, K. Fogar, J. Electrochem. Soc. 147 (2000) 3195–3205.
- [91] S.P. Jiang, Solid State Ionics 146 (2002) 1–22.
- [92] K. Chen, N. Ai, S.P. Jiang, Int. J. Hydrogen Energy 37 (2012) 10517–10525.
- [93] S.P. Jiang, W. Wang, J. Electrochem. Soc. 152 (2005) A1398–A1408.
- [94] N. Ai, S.P. Jiang, Z. Lu, K. Chen, W.H. Su, J. Electrochem. Soc. 157 (2010) B1033–B1039.
- [95] S.P. Jiang, J.G. Love, Y. Ramprakash, J. Power Sourc. 110 (2002) 201–208.
- [96] K. Chen, N. Ai, S.P. Jiang, Int. J. Hydrogen Energy 37 (2012) 1301–1310.
- [97] F.L. Liang, J. Chen, S.P. Jiang, F.Z. Wang, B. Chi, J. Pu, et al., Fuel Cells 9 (2009) 636–642.
- [98] F.L. Liang, J. Chen, B. Chi, J. Pu, S.P. Jiang, L. Jian, J. Power Sourc. 196 (2011) 153–158.
- [99] A. Hauch, S.H. Jensen, S. Ramousse, M. Mogensen, J. Electrochem. Soc. 153 (2006) A1741–A1747.
- [100] A. Hauch, S.H. Jensen, M. Mogensen, J.B. Bilde-Sørensen, J. Electrochem. Soc. 154 (2007) A619–A626.
- [101] A. Hauch, S.D. Ebbesen, S.H. Jensen, M. Mogensen, J. Electrochem. Soc. 155 (2008) B1184–B1193.

- [102] R. Barfod, M. Mogensen, T. Klemenco, A. Hagen, Y.L. Liu, P.V. Hendriksen, *J. Electrochem. Soc.* 154 (2007) B371–B378.
- [103] R. Barfod, M. Mogensen, T. Klemmense, A. Hagen, Y.L. Liu, P.V. Hendriksen, PV 2005–07, in: S.C. Singhal, J. Mizusaki (Eds.), Solid Oxide Fuel Cells (SOFC IX), The Electrochemical Society Proceedings Series, 2005, p. 524. Pennington, NJ.
- [104] C. Graves, S.D. Ebbesen, M. Mogensen, *Solid State Ionics* 192 (2011) 398–403.
- [105] R. Knibbe, M.L. Traulsen, A. Hauch, S.D. Ebbesen, M. Mogensen, *J. Electrochem. Soc.* 157 (2010) B1209–B1217.
- [106] X. Sun, M. Chen, P. Hjalmarsson, S.D. Ebbesen, S.H. Jensen, M. Mogensen, P.V. Hendriksen, *ECS Trans.* 41 (2012) 77–85.
- [107] S. Primdahl, M. Mogensen, *J. Electrochem. Soc.* 145 (1998) 2431–2438.
- [108] S. Primdahl, M. Mogensen, *J. Electrochem. Soc.* 146 (1999) 2827–2833.
- [109] M.J. Jørgensen, M. Mogensen, *J. Electrochem. Soc.* 148 (2001) A433–A442.
- [110] S. Primdahl, Risø National Laboratory, DTU, Roskilde, Denmark, 1999.
- [111] J. Schefold, M.J. Garcia, A. Brisse, D. Perednis, M. Zahid, Proceedings of the 8th European SOFC Forum, 2008, p. A1011.
- [112] J. Schefold, A. Brisse, F. Tietz, *J. Electrochem. Soc.* 159 (2012) A137–A144.
- [113] V.Ch. Kournoutis, F. Tietz, S. Bebelis, *Fuel Cells* 09 (2009) 852–860.
- [114] F. Tietz, D. Sebold, A. Brisse, J. Schefold, *J. Power Sourc.* 223 (2013) 129–135.
- [115] J. Schefold, A. Brisse, M. Zahid, *ECS Trans.* 28 (2010) 357–367.
- [116] M. Petitjean, M. Reytier, A. Chatroux, L. Bruguière, A. Mansuy, H. Sassiolas, S. Di Iorio, B. Morel, J. Mougin, *ECS Trans.* 35 (2011) 2905–2913.
- [117] S.D. Ebbesen, J. Høgh, K.A. Nielsen, J.U. Nielsen, M. Mogensen, *Int. J. Hydrogen Energy* 36 (2011) 7363–7373.
- [118] A. Brisse, J. Schefold, M. Zahid, J.U. Nielsen, P. Noyé, in: Proceedings of the 9th European SOFC Forum, 2010 (Chapter 14), pp. 49–60.
- [119] J. Schefold, A. Brisse, M. Zahid, J.P. Ouweijtjes, J.U. Nielsen, *ECS Trans.* 35 (2011) 2915–2927.
- [120] M.A. Laguna-Bercero, R. Campana, A. Larrea, J.A. Kilner, V.M. Orera, *J. Power Sourc.* 196 (2011) 8942–8947.
- [121] J. Schefold, A. Brisse, M. Zahid, *J. Electrochem. Soc.* 156 (2009) B897–B904.
- [122] S.P. Jiang, S.P.S. Badwal, *Solid State Ionics* 123 (1999) 209–224.
- [123] F. Petipas, Q. Fu, A. Brisse, C. Bouallou, *Int. J. Hydrogen Energy* 38 (2013) 2957–2964.
- [124] A. Brisse, J. Schefold, M. Zahid, *Int. J. Hydrogen Energy* 33 (2008) 5375–5382.
- [125] R. Barfod, A. Hagen, S. Ramousse, P.V. Hendriksen, M. Mogensen, *Fuel Cells* 6 (2006) 141–145.
- [126] T. Jacobsen, P.V. Hendriksen, S. Koch, *Electrochim. Acta* 53 (2008) 7500–7508.
- [127] E.C. Shin, P.A. Ahn, H.H. Seo, J.M. Jo, S.D. Kim, S.K. Woo, J.H. Yu, J. Mizusaki, J.S. Lee, *Solid State Ionics* 232 (2013) 80–96.
- [128] A. Néchache, M. Cassir, A. Ringuedé, *Int. J. Hydrogen Energy*, submitted for publication.